

Measurements of the Analyzing Power of n - ^3He
Elastic Scattering Between 1.60 and 5.54 MeV

by

James Esterline

Department of Physics
Duke University

Date: _____
Approved:

Werner Tornow, Supervisor

Haiyan Gao

Calvin R. Howell

Ronen M. Plesser

Ying Wu

Dissertation submitted in partial fulfillment of the requirements for the degree of
Doctor of Philosophy in the Department of Physics
in the Graduate School of Duke University
2012

ABSTRACT

Measurements of the Analyzing Power of n - ^3He Elastic
Scattering Between 1.60 and 5.54 MeV

by

James Esterline

Department of Physics
Duke University

Date: _____

Approved:

Werner Tornow, Supervisor

Haiyan Gao

Calvin R. Howell

Ronen M. Plesser

Ying Wu

An abstract of a dissertation submitted in partial fulfillment of the requirements for
the degree of Doctor of Philosophy in the Department of Physics
in the Graduate School of Duke University
2012

Copyright © 2012 by James Esterline
All rights reserved except the rights granted by the
Creative Commons Attribution-Noncommercial Licence

Abstract

An experiment measuring the analyzing power $A_y(\theta)$ for neutron–helium-3 (n - ^3He) elastic scattering over broad angular distributions for a range of incident neutron energies from 1.60 to 5.54 MeV has been conducted at the Triangle Universities Nuclear Laboratory. These measurements represent an effort to resolve the long-standing discrepancy between experiment and theory in low-energy three-nucleon analyzing powers, through the evaluation of analyzing powers in the four-nucleon systems, which are expected to exhibit sensitivities not accessible with fewer nucleons. The present work is described in terms of the experimental setup and data reduction techniques; a comparison of the results with rigorous calculations using both nucleon-nucleon and, as recently has become available, three-nucleon potential models is presented. While a discrepancy between calculation and measurement was observed, at low energies substantially better agreement was achieved than in related measurements of the proton–helium-3 (p - ^3He) analyzing power, suggesting a sizeable dependence on isospin in the four-nucleon systems.

To a memory

Contents

Abstract	iv
List of Tables	ix
List of Figures	x
Acknowledgements	xiii
1 Background	1
1.1 Motivation	1
1.2 History of 3NAPP and 3NF's	2
1.3 Scattering	5
1.3.1 Preliminaries	5
1.3.2 Interaction Picture Formalism	9
1.4 Theoretical Formalism for the Four-Nucleon System	13
1.5 Analyzing Power	14
1.6 Overview of Extant Data	17
2 Experimental Setup	20
2.1 Overview	20
2.2 From Polarized Ion Production to Neutron Beam Production	20
2.2.1 Overview	20
2.2.2 Ion Source	21
2.2.3 Beam Transport	26

2.2.4	Accelerator	28
2.2.5	Neutron Beam Production	29
2.3	Targets and Detectors	30
2.3.1	Overview	30
2.3.2	^3He Gas Scintillator	31
2.3.3	^4He Gas Scintillator	33
2.3.4	Neutron detectors	34
3	Electronics	36
3.1	Overview	36
3.1.1	Description of Quantities of Interest	37
3.2	Description of Implementation	37
3.2.1	Common Elements	37
3.2.2	Spin-State and Beam-Current Electronics	39
3.2.3	Primary array electronics	40
3.2.4	Polarimeter Electronics	42
3.3	Trigger Supervision and Data Acquisition	45
4	Experimental Synopsis	48
4.1	Overview	48
4.2	Summary of Data	48
5	Data Reduction and Analysis	54
5.1	Overview	54
5.2	Description of Methods	56
5.2.1	Primary Array	56
5.2.2	Polarimeter	60

6	Monte Carlo Simulations	63
6.1	Monte Carlo Simulations and Corrections	63
7	Results and Summary	71
7.1	Presentation of Data	71
7.2	Discussion of Results	72
7.3	Comparison with Previous Measurements	80
7.4	Comparison with Related Systems	81
7.5	Summary	82
	Bibliography	86
	Biography	89

List of Tables

1.1	Prior Measurements in Related Four-Nucleon Systems	18
1.2	Prior Measurements in the $n-^3\text{He}$ System	19
2.1	RF Settings for Neutron Polarization States	25
2.2	Operating Parameters for the Deuterium Gas Cell	31
2.3	Operating Parameters for the Tritiated Titanium Target	31
4.1	Catalogue of Runs Conducted While Using the DAQ4 Workstation	50
4.2	Catalogue of Runs Conducted While Using the DAQ2 Workstation	51
4.3	Additional Exclusions for Run Catalogues	52
4.4	Exposure Times per Angle and Energy	53
6.1	A summary of interaction designations for double scattering in the Monte Carlo simulation.	65
7.1	Uncorrected (“raw”) results from data analysis for the $n-^3\text{He}$ analyzing power at all energies and angles entailed by the present work; where available, the center-of-mass angles for 3.14 MeV are used as approximations for those at other energies. ΔA_y denotes the statistical uncertainty in the given values.	73
7.2	Inferred point geometry results of the present experiment, obtained by applying multiplicative corrections determined from Monte Carlo simulations, presented as in Table 7.1.	74

List of Figures

1.1	Feynman Diagrams of Interactions in a Modern NN Potential Model	3
1.2	Feynman Diagrams of Interactions in a Modern 3NF Potential Model	4
1.3	3NF Contributions to NN Calculations of $p-d$ $A_y(\theta)$	6
1.4	Comparison of the Effects of the Inclusion of Different 3NF's on $p-d$ $A_y(\theta)$	7
2.1	Atomic Beam Polarized Ion Source (ABPIS)	23
2.2	Breit-Rabi Diagram for Protium	24
2.3	Breit-Rabi Diagram for Deuterium	25
2.4	Beam Transport	28
2.5	Deuterium Gas Target	30
2.6	Tritiated Titanium Target	30
2.7	Scatterer and Detector Layout	32
2.8	^3He Gas Scintillator	33
2.9	^4He Gas Scintillator	34
2.10	Liquid Scintillator Neutron Detector	35
3.1	Block diagram of the electronics for the spin state electronics.	41
3.2	Block diagram of the electronics for the primary array. Dotted rectangles refer by name to elements either described in other figures in this section or to a collection of similar elements not explicitly presented in the figure. Here, the electronics for only one side detector are shown, as the design was general. The OR used to generate the primary array trigger is of all center-side coincidences.	43

3.3	Detail of the electronics for the primary array trigger. The TDC here doubled corresponds to the distinct elements for PSD and flight-time as presented in the preceding figure; in reality, only one TDC module was employed. While it is not shown here to avoid cluttering, the VME busy signal is a product of the JLab trigger supervisor module.	44
3.4	Block diagram of the electronics for the polarimeter.	46
3.5	Detail of the electronics for the polarimeter array trigger. As before, the Silena used was a single module, and took a single common gate, hence the depiction.	47
5.1	Pulse-Shape Discrimination	57
5.2	Flight-Time Selection	59
5.3	Fit to the Helium Recoil Energy Distribution	61
5.4	Helium Recoil Energy Selection	62
6.1	Above, the fiducial (“point geometry”) analyzing power and, below, the differences between it and results of Monte Carlo simulation for $E_n = 1.60$ MeV including (“full MC”) and excluding (“finite geometry”) multiple scattering contributions. It is noted that differences are roughly an order of magnitude less than values, as prompted this mode of presentation. The magnitude of the differences for this energy in particular is due to a shorter target-detector distance and a corresponding exacerbation of finite-geometry effects.	66
6.2	Fiducial analyzing power and differences as in Fig. 6.1, for $E_n = 2.26$ MeV.	67
6.3	Fiducial analyzing power and differences as in Fig. 6.1, for $E_n = 3.14$ MeV.	68
6.4	Fiducial analyzing power and differences as in Fig. 6.1, for $E_n = 4.05$ MeV.	69
6.5	Fiducial analyzing power and differences as in Fig. 6.1, for $E_n = 5.54$ MeV.	70
7.1	The n - ^3He analyzing power at $E_n = 1.60$ MeV measured in the present work (“TUNL data”), including multiplicative corrections determined from Monte Carlo simulations, along with theoretical calculations using the Argonne v18 and CD-Bonn N - N potential models, as well as the latter supplemented by a Δ -mediated $3N$ potential.	75

7.2	Measurement and theoretical calculation for the n - ^3He analyzing power at $E_n = 2.26$ MeV as presented in Fig. 7.1.	76
7.3	Measurement and theoretical calculation for the n - ^3He analyzing power at $E_n = 3.14$ MeV as presented in Fig. 7.1.	77
7.4	Measurement and theoretical calculation for the n - ^3He analyzing power at $E_n = 4.05$ MeV as presented in Fig. 7.1.	78
7.5	Measurement and theoretical calculation for the n - ^3He analyzing power at $E_n = 5.54$ MeV as presented in Fig. 7.1.	79
7.6	Differences between experimental and theoretical values of the n - ^3He analyzing power at $E_n = 1.60$ MeV (actual values as in Fig. 7.1). . .	80
7.7	Differences between experimental and theoretical values of the n - ^3He analyzing power at $E_n = 2.26$ MeV (actual values as in Fig. 7.2). . .	81
7.8	Differences between experimental and theoretical values of the n - ^3He analyzing power at $E_n = 3.14$ MeV (actual values as in Fig. 7.3). . .	82
7.9	Measurement minus calculations at $E_n = 4.05$ MeV	83
7.10	Measurement minus calculations at $E_n = 5.54$ MeV	83
7.11	Comparison with Previous Measurement at $E_n = 3.7$ MeV	84
7.12	Comparison Between Different 4N Systems	85

Acknowledgements

I would like to acknowledge funding from the Department of Energy (fund code DE-FG02-97ER41033) which enabled the present work; my parents, Albert and Maureen Esterline, for having me and paving the way for my success through years of upbringing; my many friends here at Duke for their enduring support—particularly the “Nerd Night” crowd of Nasser Demir, Mary Kidd, and (most helpfully these last few years) Jonathan Cranford, but also fellow incoming classmates Kenneth Mackenzie, Peng Li, and Arya Roy, for years of thought-provocation (for better or worse); TUNL’s rainmaker when it came to polarized beams, John Dunham; my many mentors here at TUNL, starting with Gary Weisel, and—though it does many a disservice to limit the names to so few—particularly Calvin Howell and Alex Crowell, the latter even more so for his patient assistance during the preparation of this document. I owe special thanks to the surgeons whose work has enabled me to see this day, Andrew Lodge and Betty Tong; and more than I can comprehend to the Lord Almighty. But, at the risk of extending this past the Omega, I reserve my greatest appreciation on this Earth to my advisor, Werner Tornow, for his patience, candid advice, and tireless support throughout all my years as a graduate student.

And to the many others I owe, without whom (as without those above) I would not be writing this today, and thus wrong in omitting your names: know that you have no less place in my mind or heart for it, that your every contribution—be it material, conceptual, spiritual, emotional—was, has been, and will always be appreciated.

Background

1.1 Motivation

The physics of atomic nuclei is dominated by the strong interaction, understood at the fundamental level as the quantum chromodynamics of color-charge-carrying quarks and gluons. While this theory is strongly supported by a variety of experimental results, it is presently limited in applicability due to the observed property of confinement—that, except at extremely small length scales or extreme thermodynamic conditions, strongly interacting matter occurs only in color-neutral (“white”) systems—as the quantum theory of fields in which chromodynamics is formulated is at present unable fully to address the behavior of bound states. Interactions among even the simplest (at least nearly) stable bound states, the proton and the neutron (collectively referred to as nucleons), are therefore currently treated with more phenomenological models.

The resulting nucleon-nucleon (NN) potentials, prominently including contributions from the exchange of mesons, themselves do not completely determine the dynamics of larger nuclear systems. (An example of such an interaction is that ob-

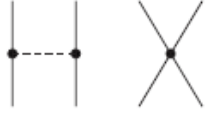
tained in chiral perturbation theory for which the Feynman diagrams contributing to the presently most comprehensive treatment are shown in Fig. 1.1.) Contributions to the nuclear potential not reducible to NN interactions among constituent nucleons are categorized as n -nucleon forces, with the three-nucleon force (3NF) describing the entire such component of the three-nucleon interaction, the four-nucleon force (4NF) that of the four-nucleon interaction not reducible to either constituent NN or 3NF-mediated interactions, and so forth. (The Feynman diagrams for the 3NF obtained as in the previous example are shown in Fig. 1.2.)

Interest in the present experiment is motivated by a long-standing problem in the realm of few-nucleon physics, the three-nucleon analyzing power puzzle (3NAPP), which entails discrepancies between calculation and measurement of neutron-deuteron and proton-deuteron analyzing powers (specifically A_y). While the three-nucleon system is a more obvious venue for an investigation of 3NF, to the incomplete understanding of which is presently ascribed the 3NAPP, the preponderance of A_y measurements in the three-nucleon system which have thus far eluded theoretical efforts suggest the need for a different approach to better 3NF models. Due to the extreme smallness of calculated 4NF's at low energies (as indicated by [Del08] for a Δ -mediated 4NF and by [Epe06] in chiral effective field theory), and spin-isospin structures not available with fewer nucleons, the four-nucleon system becomes a natural choice.

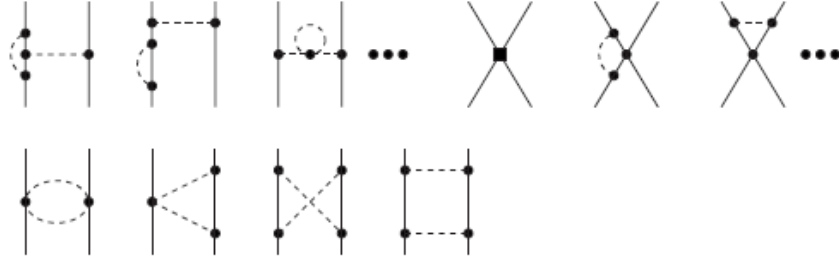
1.2 History of 3NAPP and 3NF's

In the interest of providing a possibly insightful perspective on the development of theoretical models and the experimental database, it may be noted that the 3NAPP arose when the first rigorous three-nucleon calculation using the Paris NN potential in Fadeev equations was found in 1987 to be in disagreement with (and notably falling short of) n - d analyzing power measurements for neutron energies between 10

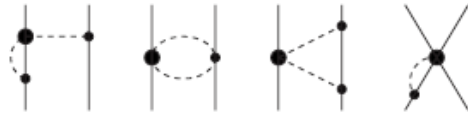
Leading order



Next-to-leading order



Next-to-next-to-leading order



Next-to-next-to-next-to-leading order

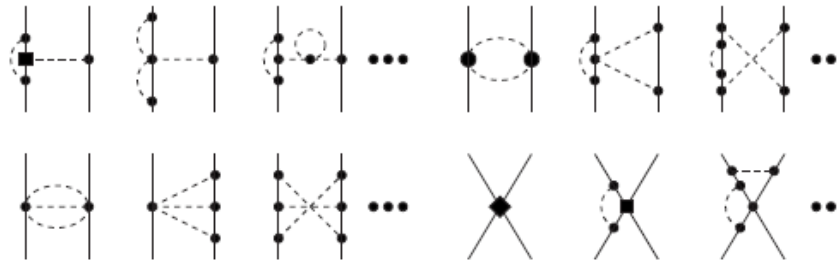
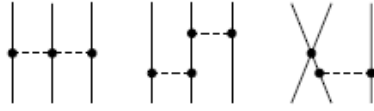
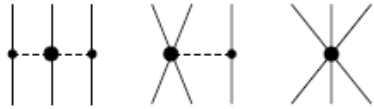


FIGURE 1.1: Interactions to next-to-next-to-next-to-leading order (N^3LO) in chiral perturbation theory, as represented by their Feynman diagrams, which contribute to the NN potential (as given in [Epe09], whence this graph was obtained). Solid lines indicate nucleons, dashed lines pions; vertices are, in increasing order of an index Δ' given by the sum of the number of derivatives and powers of pion mass with half the number of nucleon fields: dots, filled circles, filled squares, and filled diamonds for $\Delta' = 2, 3, 4,$ and $5,$ respectively.

Next-to-leading order



Next-to-next-to-leading order



Next-to-next-to-next-to-leading order

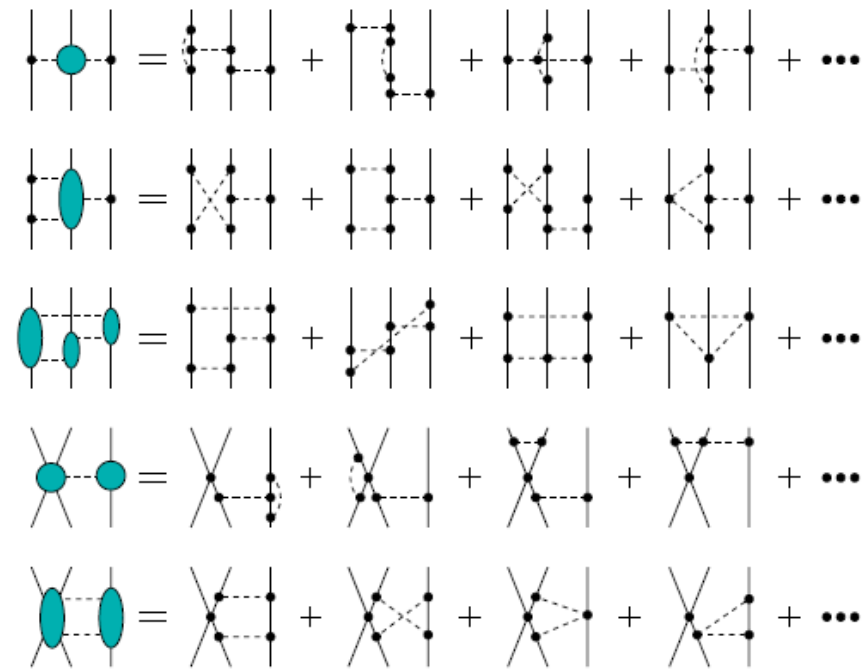


FIGURE 1.2: Interactions to $N^3\text{LO}$ in chiral perturbation theory, as represented by their Feynman diagrams, which contribute to the 3NF (as given in [Epe09], whence again this graph was obtained). Lines and vertices are as in Fig. 1.1; the $N^3\text{LO}$ interactions are grouped according to common topology.

and 14 MeV. When similar discrepancies were found at other low energies (under about 35 MeV for n - d A_y 's, p - d predictions being then unavailable due to difficulties in incorporating the Coulomb interaction), with predictions of analyzing power maxima underestimating measured values by a quarter to a third for E_n between 5 and 14 MeV, and in light of cross sections and binding energies being also (if less dramatically) underpredicted, it was hoped that the inclusion of 3NF's could rectify the situation. That expectation was quashed in the 1990's as rigorous calculations involving first the Tucson-Melbourne (TM) current-algebra-derived 3NF in 1993, and later those involving other 3NF models, including the introduction of a phenomenological repulsive core in the Urbana 3NF's and the inclusion of intermediate Δ excitations, were unable to resolve the discrepancy in analyzing power despite success in emending binding energies and cross sections (albeit with some exceptions in the latter, such as the "space star" configuration in n - d breakup). While the development of the 3NAPP had to this point concerned the n - d system, the first successful treatments of the Coulomb interaction in p - d scattering revealed similar differences between theory and experiment, as shown in Fig. 1.3; in both this figure and Fig. 1.4, the extension to p - d scattering of the insufficiency of various 3NF models in resolving the discrepancy is also exhibited.

1.3 Scattering

1.3.1 Preliminaries

The quantum mechanical formalism of scattering, in the non-relativistic regime adequate for the present experiment, may be developed from the Schrödinger equation (Eq. 1.1) describing the evolution of a state vector $|\Psi\rangle$ under the influence of a Hamiltonian H :

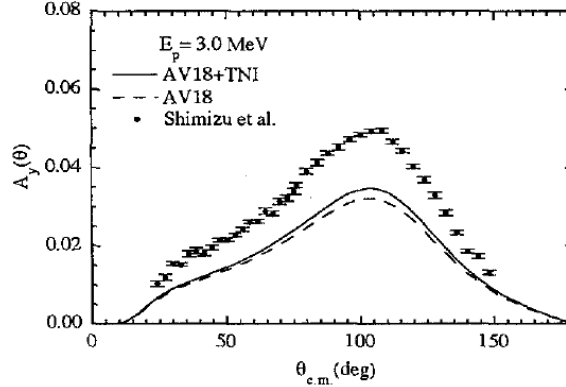


FIGURE 1.3: The analyzing power of elastic p - d scattering at $E_p = 3.0$ MeV, comparing measurements from [Shi95] to theoretical calculations using the Argonne v.18 (AV18) NN potential model by itself (dashed line) and in conjunction with the Urbana IX (UIX, though here referred to as TNI—“three nucleon interaction”) 3NF (solid line) from [Kie96]; the graph is a slight modification of one from this latter source. The only very slight improvement in agreement between theory and experiment resulting from the inclusion of the 3NF is noted.

$$i\hbar \frac{d}{dt} |\Psi(t)\rangle = H |\Psi(t)\rangle . \quad (1.1)$$

For the purpose of scattering, the free Hamiltonian H_0 of Eq. 1.2 is *sine qua non*:

$$H_0 = -\frac{\hbar^2}{2m} \nabla^2 , \quad (1.2)$$

as are its eigenfunctions, the plane waves (here indexed by momentum) $\psi_{\vec{p}}$, as given in Eq. 1.3:

$$\psi_{\vec{p}} = N \exp\left(\frac{i\vec{p} \cdot \vec{r}}{\hbar}\right) , \quad (1.3)$$

which correspond to energy eigenvalues of $(2m)^{-1} p^2$, and are here left with arbitrary normalization. (Henceforth, the spatial frequency $k = \hbar^{-1}p$ will be used in place of the momentum.)

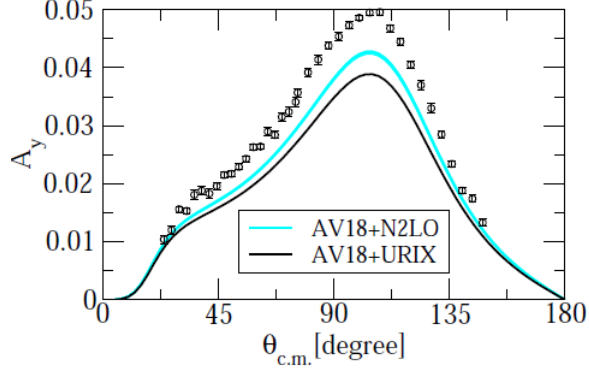


FIGURE 1.4: As in Fig. 1.3, with the same experimental data compared to calculations incorporating both the same AV18+UIX combination and AV18 in conjunction with a more recently developed 3NF containing terms to next-to-subleading order in chiral effective theory from [Nav07]; both calculations and graph, again slightly modified, are from [Kie10]. While the lessening of discrepancy due to the inclusion of the new 3NF is somewhat more marked than that for UIX, it is noted that this newer calculation remains well out of agreement with experimental data.

One approach to a general solution of the Schrödinger equation for $H = H_0 + V$ (for a simplified case neglecting spin) is to apply Green's function methods to the eigenvalue equation for a free Hamiltonian (equivalent to the Helmholtz equation), thereby treating $V\psi$ as a source term and thus yielding an implicit equation for ψ . The differential equation so described is Eq. 1.4:

$$\begin{aligned}
 (H_0 - E) \psi(\vec{r}) &= & (1.4) \\
 - \left(\frac{\hbar^2}{2m} \nabla^2 + E \right) \psi(\vec{r}) &= -V(\vec{r}) \psi(\vec{r}); \\
 \therefore (\nabla^2 + k^2) \psi(\vec{r}) &= U(\vec{r}) \psi(\vec{r}) ,
 \end{aligned}$$

where $U = 2m\hbar^{-2}V$ and $k = (2m\hbar^{-2}E)^{1/2}$; the desired Green's function $G_{\vec{k}}(\vec{r}, \vec{r}')$ must satisfy Eq. 1.5:

$$(\nabla^2 + k^2) G_{\vec{k}}(\vec{r}, \vec{r}') = \delta(\vec{r} - \vec{r}') . \quad (1.5)$$

Two linearly independent solutions, identified as the advanced and retarded Green's functions, to Eq. 1.5 are given by Eqs. 1.6 and 1.7, respectively:

$$G_{\vec{k}}^+(\vec{r}, \vec{r}') = -\frac{\exp(ik|\vec{r} - \vec{r}'|)}{4\pi|\vec{r} - \vec{r}'|}, \quad (1.6)$$

$$G_{\vec{k}}^-(\vec{r}, \vec{r}') = -\frac{\exp(-ik|\vec{r} - \vec{r}'|)}{4\pi|\vec{r} - \vec{r}'|}. \quad (1.7)$$

Application of a radial momentum operator on these Green's functions reveals that the advanced is an eigenstate with positive eigenvalue, and that the retarded is an eigenstate with negative eigenvalue. Thus, while a general solution to Eq. 1.4 could contain contributions from both Green's functions, the non-existence of collapsing circular waves results in Eq. 1.8 representing the general solution of importance to scattering:

$$\psi_{\vec{k}}^{(+)}(\vec{r}) = N \exp(i\vec{k} \cdot \vec{r}) - \int d^3r' \frac{\exp(ik|\vec{r} - \vec{r}'|)}{4\pi|\vec{r} - \vec{r}'|} U(\vec{r}') \psi_{\vec{k}}^{(+)}(\vec{r}'). \quad (1.8)$$

For the purposes of extracting a cross section, Eq. 1.8 can be approximately expressed in the form of Eq. 1.9:

$$\psi_{\vec{k}}^{(+)}(\vec{r}) \simeq N \left(\exp(i\vec{k} \cdot \vec{r}) + \frac{f_k(\hat{r})}{r} \exp(ikr) \right), \quad (1.9)$$

importantly with equality holding to $\mathcal{O}(r^{-1})$ as $r \rightarrow \infty$; the quantity $f_k(\hat{r})$ is the scattering amplitude, for which an expression (Eq. 1.10) in terms of $\psi^{(+)}$ may be obtained by comparing Eqs. 1.8 and 1.9, using the approximation, valid for large r , $|\vec{r} - \vec{r}'| \simeq r - \hat{r} \cdot \vec{r}'$:

$$f_k(\hat{r}) = -\frac{1}{4\pi N} \int \exp(-k\hat{r} \cdot \vec{r}') d^3r' U(\vec{r}') \psi^{(+)}(\vec{r}'), \quad (1.10)$$

which directly relates to the differential cross section by Eq. 1.11:

$$\frac{d\sigma}{d\Omega} = |f_k(\hat{r})|^2 . \quad (1.11)$$

1.3.2 Interaction Picture Formalism

In order to connect the incoming and outgoing free-particle solutions, the interaction picture definition Eq. 1.12 provides a starting point:

$$|\tilde{\Psi}(t)\rangle = \exp\left(\frac{iH_0t}{\hbar}\right) |\Psi(t)\rangle , \quad (1.12)$$

where $|\tilde{\Psi}\rangle$ is the interaction-picture state vector, H_0 is the free Hamiltonian (i.e., the kinetic term, $-\frac{\hbar^2}{2m}\nabla^2$),¹ and $|\Psi\rangle$ is the Schrödinger-picture state vector as defined by Eq. 1.1. The time derivative of $|\tilde{\Psi}\rangle$ yields Eq. 1.13:

$$\begin{aligned} i\hbar \frac{d}{dt} |\tilde{\Psi}(t)\rangle &= -H_0 |\tilde{\Psi}(t)\rangle + \exp\left(\frac{iH_0t}{\hbar}\right) H |\Psi(t)\rangle \\ &= \exp\left(\frac{iH_0t}{\hbar}\right) V \exp\left(\frac{-iH_0t}{\hbar}\right) |\Psi(t)\rangle \\ &\equiv \tilde{V}(t) |\Psi(t)\rangle . \end{aligned} \quad (1.13)$$

The resulting time-evolution operator $\tilde{T}(t, t_0)$ (for which $\tilde{T}(t_b, t_a) |\tilde{\Psi}(t_a)\rangle = |\tilde{\Psi}(t_b)\rangle$) in the interaction picture that is given by Eq. 1.14:

$$\begin{aligned} \tilde{T}(t, t_0) &= \tilde{T}(t_0, t_0) + \int_{t_0}^t \frac{d}{dt'} \tilde{T}(t', t_0) dt' \\ &= 1 - \frac{i}{\hbar} \int_{t_0}^t \tilde{V}(t') \tilde{T}(t', t_0) dt' , \end{aligned} \quad (1.14)$$

¹ For more general purposes of the interaction picture, H_0 is identified as any particularly tractable “model Hamiltonian” which can be isolated from the full Hamiltonian.

where $\frac{d}{dt'}\tilde{T}(t', t_0)$ is obtained from $\frac{d}{dt'}\left|\tilde{\Psi}(t')\right\rangle = \frac{d}{dt'}\tilde{T}(t', t_0)\left|\tilde{\Psi}(t_0)\right\rangle$; the matrix elements of \tilde{T} are shown in Eq. 1.15:

$$\begin{aligned}\langle f|\tilde{T}(t, t_0)|i\rangle &= \delta_{fi} - \frac{i}{\hbar} \int_{t_0}^t \langle f|\tilde{V}(t')\tilde{T}(t', t_0)|i\rangle dt' \\ &= \delta_{fi} - \frac{i}{\hbar} \int_{t_0}^t \langle f|\exp\left(\frac{iH_0t'}{\hbar}\right)V\exp\left(\frac{-iH_0t'}{\hbar}\right)\left(\sum_n|n\rangle\langle n|\right)\tilde{T}(t', t_0)|i\rangle dt' \\ &= \delta_{fi} - \frac{i}{\hbar} \sum_n \langle f|V|n\rangle \int_{t_0}^t \exp(i\omega_{fn}t') \langle n|\tilde{T}(t', t_0)|i\rangle dt',\end{aligned}\quad (1.15)$$

where $\hbar\omega_{ab} \equiv E_a - E_b$. For scattering, an initial state taking the form of an incident plane wave in the arbitrary past (which the ideal treatment extends to the infinite past) time-evolves to obtain an outgoing final state (and hence a scattering amplitude); the desired quantity is the scattering matrix S_{fi} in Eq. 1.16:

$$S_{fi} = \langle f|\tilde{T}(+\infty, -\infty)|i\rangle. \quad (1.16)$$

To obtain amplitudes from the time evolution matrix elements in Eq. 1.15, as well as provide a well-defined evolution from infinite past, the Ansatz of Eq. 1.17 (following [Mer98]) is made:

$$\langle f|\tilde{T}(t, -\infty)|i\rangle = \delta_{fi} - \frac{i}{\hbar} T_{fi} \lim_{\epsilon \rightarrow 0^+} \left(\lim_{t_0 \rightarrow -\infty} \int_{t_0}^t \exp(i\omega_{fi}t' + \epsilon t') dt' \right), \quad (1.17)$$

where the order of limits is to be strictly maintained.² Taking the t_0 limit explicitly yields Eq. 1.18:

$$\langle f|\tilde{T}(t, -\infty)|i\rangle = \delta_{fi} - \frac{1}{\hbar} T_{fi} \lim_{\epsilon \rightarrow 0^+} \frac{\exp(i\omega_{fi}t + \epsilon t)}{\omega_{fi} - i\epsilon}. \quad (1.18)$$

² A further restriction that $|t| \ll \frac{1}{\epsilon}$ may be specified to avoid confusion when taking the ultimately desired limit of $t \rightarrow \infty$

To connect this result to S_{fi} , the limit $t \rightarrow \infty$ merits scrutiny; identifying the result as a δ function via Eq. 1.19:

$$\lim_{\substack{(T \rightarrow \infty) \\ (\epsilon \rightarrow 0^+) | \epsilon T \rightarrow 0}} \frac{\exp(i(\omega_{fi} + \epsilon)T)}{\omega_{fi} - i\epsilon} = 2\pi i \delta(\omega) \ , \quad (1.19)$$

resulting in Eq. 1.20:

$$\begin{aligned} S_{fi} &= \delta_{fi} - \frac{i}{\hbar} T_{fi} \delta(\omega_{fi}) \\ &= \delta_{fi} - iT_{fi} \delta(E_{fi}) \ , \end{aligned} \quad (1.20)$$

which (particularly in conjunction with the observation that, except for $|i\rangle = |f\rangle$), the time derivative of the norm $|\langle f | \tilde{T}(t, -\infty) | i \rangle|$ approaches a constant with vanishing ϵ) provides a physical interpretation of T_{fi} as quantifying the transition rate from state $|i\rangle$ into state $|f\rangle$.

Substituting the expression for \tilde{T} from Eq. 1.18 in Eq. 1.15 (with t_0 taken to $-\infty$) yields 1.21 (with the $\epsilon \rightarrow 0^+$ limit implicit throughout and furthermore validly introduced to Eq. 1.15):

$$\begin{aligned} \langle f | \tilde{T}(t, -\infty) | i \rangle &= \delta_{fi} - \frac{1}{\hbar} T_{fi} \frac{\exp(i\omega_{fi}t + \epsilon t)}{\omega_{fi} - i\epsilon} \\ &= \delta_{fi} - \frac{i}{\hbar} \langle f | V | i \rangle \int_{-\infty}^t \exp(i\omega_{fi}t' + \epsilon t') dt' \\ &\quad + \frac{i}{\hbar^2} \sum_n \langle f | V | n \rangle T_{ni} \int_{-\infty}^t \exp(i\omega_{fn}t' + \epsilon t') \left(\frac{\exp(i\omega_{ni}t' + \epsilon t')}{\omega_{ni} - i\epsilon} \right) dt' \\ &= \delta_{fi} - \frac{i}{\hbar} \left(\langle f | V | i \rangle - \frac{1}{\hbar} \sum_n \langle f | V | n \rangle \frac{T_{ni}}{\omega_{ni} - i\epsilon} \right) \frac{\exp(i\omega_{fi}t + \epsilon t)}{\omega_{fi} - i\epsilon} \ , \end{aligned} \quad (1.21)$$

where the irrelevancy of positive m enables the factorization. Comparison of the top and bottom lines yields Eq. 1.22:

$$T_{fi} = \langle f | V | i \rangle - \frac{1}{\hbar} \sum_n \langle f | V | n \rangle \frac{T_{ni}}{\omega_{ni} - i\epsilon} . \quad (1.22)$$

As the matrix elements of time-evolution operator \tilde{T} could be represented as the inner product of two physically meaningful states, namely $\left\{ \left| \tilde{\Psi}(t) \right\rangle \right\}$ for various values of t , the pursuit of a similar interpretation for the transition matrix, i.e., of the state $|\Phi\rangle$ for which $T_{fi} = \langle f | \Phi \rangle$, yields Eq. 1.23:

$$\langle f | \Phi \rangle = \langle f | V | i \rangle - \frac{1}{\hbar} \sum_n \langle f | V | n \rangle \frac{\langle n | \Phi \rangle}{\omega_{ni} - i\epsilon} . \quad (1.23)$$

As this holds for any $|f\rangle$, the duals can be dropped, yielding Eq. 1.24:

$$\begin{aligned} |\Phi\rangle &= V | i \rangle - \frac{1}{\hbar} \sum_n V | n \rangle \frac{\langle n | \Phi \rangle}{\omega_{ni} - i\epsilon} \\ &= V | i \rangle - \frac{1}{\hbar} \sum_n V \frac{1}{E_i - H_0 - i\epsilon} | n \rangle \langle n | \Phi \rangle \\ &= V | i \rangle - \frac{1}{\hbar} V \frac{1}{E_i - H_0 - i\epsilon} |\Phi\rangle , \end{aligned} \quad (1.24)$$

where the introduction of the operator $(E_i - H_0 - i\epsilon)^{-1}$ has enabled the collapse of the sum over the complete set $\{|n\rangle\}$. As this operator is a representation of the advanced Green's function of the free Hamiltonian (more accurately, the resolvent of H_0), there is a parallel to Eq. 1.8 made more direct by the substitution of $V |\Psi^{(+)}\rangle$ for $|\Phi\rangle$,³ resulting in the Lippmann-Schwinger equation (Eq. 1.25):

³ To eliminate confusion, left-multiplication of Eq. 1.24 by V^{-1} following this substitution results in Eq. 1.25.

$$|\Psi^{(+)}\rangle = |i\rangle + G^+(E_i) V |\Psi^{(+)}\rangle , \quad (1.25)$$

where $G^+(E_i) = (E_i - H_0 - i\epsilon)^{-1}$.

1.4 Theoretical Formalism for the Four-Nucleon System

Although there are other theoretical treatments of the four-nucleon system that produce calculably reliable results (most notable the Faddeev-Yakubovsky equations and the method of hyperspherical harmonics), only the Alt-Grassberger-Sandhas (AGS) equations, originally from [Gra67], are here presented; these equations express transition operators in the four-nucleon system in terms of those of the constituent two-nucleon interactions. For n - ^3He scattering (following the notation of [Viv11]), transition operators \mathcal{U} between two partitions of the four nucleon system denoted 3+1 and 2+2 (into a cluster of three nucleons—labeled 1 through 3—plus a free nucleon, 4; and two clusters of two nucleons apiece—label 1 with label 2 and 3 with 4—respectively) are defined by the integral equations 1.26 and 1.27:

$$\mathcal{U}_{3+1;3+1} = - (G_0 T G_0)^{-1} P_{34} - P_{34} U_1 G_0 T G_0 \mathcal{U}_{3+1;3+1} + U_2 G_0 T G_0 \mathcal{U}_{2+2;3+1} , \quad (1.26)$$

$$\mathcal{U}_{2+2;3+1} = (G_0 T G_0)^{-1} (\mathbb{1} - P_{34}) + (\mathbb{1} - P_{34}) U_1 G_0 T G_0 \mathcal{U}_{3+1;3+1} , \quad (1.27)$$

where T is the two-nucleon transition matrix, G_0 is the free resolvent (namely $(E - H_0 + i\epsilon)^{-1}$, for E the energy of the four nucleon system), P_{ij} is the permutation of nucleons with the i and j labels, $U_{i\in 1,2}$ is given by Eq. 1.28:

$$U_i = P_i G_0^{-1} + P_i T G_0 U_i , \quad (1.28)$$

where $P_1 = P_{12}P_{23} + P_{13}P_{23}$ and $P_2 = P_{13}P_{24}$.

T is itself determined by the application of the implicit relation Eq. 1.29:

$$T = V_{NN} + V_{NN} G_0 T , \quad (1.29)$$

where V_{NN} is the nucleon-nucleon potential.

1.5 Analyzing Power

The definition of the analyzing power A for a given direction \hat{v} , is given by Eq. 1.30:

$$A = \frac{\text{Tr} (M \hat{v} \cdot \vec{\sigma} M^\dagger)}{\text{Tr} (M M^\dagger)} , \quad (1.30)$$

where $\vec{\sigma}$ is the vector of Pauli matrices ($\sigma_1 (= \sigma_x)$, $\sigma_2 (= \sigma_y)$, $\sigma_3 (= \sigma_z)$) acting on only the incident particle spin; M is the transition matrix with explicit spin dependence (typically including the normalization to the scattering amplitude). This gives the analyzing power A_y in the \hat{y} direction explicitly as Eq. 1.31:

$$A_y = \frac{\text{Tr} (M \sigma_y M^\dagger)}{\text{Tr} (M M^\dagger)} . \quad (1.31)$$

Eq. 1.31 reduces to a relative difference, Eq. 1.32, of differential cross sections for different incident spin projections along the \hat{y} direction (noting that σ_y is $\text{diag} (1, -1)$ in the basis of spin projections along the \hat{y} axis):

$$A_y (\theta) = \frac{\frac{d\sigma}{d\Omega_\uparrow} (\theta) - \frac{d\sigma}{d\Omega_\downarrow} (\theta)}{\frac{d\sigma}{d\Omega_\uparrow} (\theta) + \frac{d\sigma}{d\Omega_\downarrow} (\theta)} , \quad (1.32)$$

where the subscripts label only the incident spin, and the dependence on scattering angle has been made explicit; the azimuthal angle is understood to be zero, restricting

the scattering (semi-)plane under consideration to be perpendicular to the selected spin direction.

To relate this quantity to the enumerations directly obtained in particle detection, it must be expressed in terms of the apparent differential cross sections for a given polarization state of an incident ensemble. These apparent cross sections, here denoted by $\frac{d\sigma}{d\Omega_p}$, are given by Eq. 1.33:

$$\frac{d\sigma}{d\Omega_p} = \text{Tr} (M\rho M^\dagger), \quad (1.33)$$

where ρ is the density matrix of the incident ensemble. For a polarization vector \vec{p} being the expectation value of particle spins, the density matrix is in turn given by Eq. 1.34:

$$\rho = \frac{1 + \vec{p} \cdot \vec{\sigma}}{2}. \quad (1.34)$$

Evaluating the trace in Eq. 1.33 over the incident spins for an ensemble polarization $\vec{p} = p\hat{y}$ yields Eq. 1.35:

$$\frac{d\sigma}{d\Omega_p}(\theta, \phi) = \frac{1+p}{2} \frac{d\sigma}{d\Omega_\uparrow}(\theta, \phi) + \frac{1-p}{2} \frac{d\sigma}{d\Omega_\downarrow}(\theta, \phi), \quad (1.35)$$

where the angular dependence once again has just been made explicit. As, through rotational invariance, the simultaneous inversion of the spin in the \hat{y} direction and a shift in azimuthal angle by π provides the identity in Eq. 1.36:

$$\frac{d\sigma}{d\Omega_\uparrow}(\theta, \phi) = \frac{d\sigma}{d\Omega_\downarrow}(\theta, \phi \pm \pi), \quad (1.36)$$

Eq. 1.35 can be expressed solely in terms of $\frac{d\sigma}{d\Omega_\uparrow}$ in Eq. 1.37:

$$\frac{d\sigma}{d\Omega_p}(\theta, \phi) = \frac{1+p}{2} \frac{d\sigma}{d\Omega_\uparrow}(\theta, \phi) + \frac{1-p}{2} \frac{d\sigma}{d\Omega_\uparrow}(\theta, \phi \pm \pi). \quad (1.37)$$

As the analyzing power involves only the $x-z$ scattering plane, and for notational convenience, the angle about the \hat{y} axis from the \hat{z} axis replaces the polar-azimuthal pair in the following; thus, $(\theta, \phi \pm \pi)$ hereafter appears as merely $-\theta$. The sums and differences of the apparent differential cross sections at $\pm\theta$ thus simplify to Eqs. 1.38 and 1.39:

$$\frac{d\sigma}{d\Omega_p}(\theta) + \frac{d\sigma}{d\Omega_p}(-\theta) = \frac{d\sigma}{d\Omega_\uparrow}(\theta) + \frac{d\sigma}{d\Omega_\uparrow}(-\theta), \quad (1.38)$$

$$\frac{d\sigma}{d\Omega_p}(\theta) - \frac{d\sigma}{d\Omega_p}(-\theta) = p \left(\frac{d\sigma}{d\Omega_\uparrow}(\theta) - \frac{d\sigma}{d\Omega_\uparrow}(-\theta) \right). \quad (1.39)$$

By the identity in Eq. 1.36, the analyzing power as given in Eq. 1.32 may thus be identified in Eq. 1.40:

$$A_y(\theta) = \frac{1}{p} \frac{\frac{d\sigma}{d\Omega_p}(\theta) - \frac{d\sigma}{d\Omega_p}(-\theta)}{\frac{d\sigma}{d\Omega_p}(\theta) + \frac{d\sigma}{d\Omega_p}(-\theta)}, \quad (1.40)$$

where p is the polarization of the incident beam in the \hat{y} direction (where the beam itself, or rather its momentum, is understood to be in the \hat{z} direction). As the relative difference in differential cross sections is proportional to the polarization, this normalization results in a polarization-independent quantity.

For the purposes of this measurement, during which the spin polarization was frequently intentionally reversed, an equivalent value of the analyzing power was obtained using Eq. 1.41:

$$A_y = \frac{1}{p} \frac{\sqrt{\frac{\frac{d\sigma}{d\Omega}_{p_\uparrow}(\theta) \frac{d\sigma}{d\Omega}_{p_\downarrow}(-\theta)}{\frac{d\sigma}{d\Omega}_{p_\downarrow}(\theta) \frac{d\sigma}{d\Omega}_{p_\uparrow}(-\theta)} - 1}}{\sqrt{\frac{\frac{d\sigma}{d\Omega}_{p_\uparrow}(\theta) \frac{d\sigma}{d\Omega}_{p_\downarrow}(-\theta)}{\frac{d\sigma}{d\Omega}_{p_\downarrow}(\theta) \frac{d\sigma}{d\Omega}_{p_\uparrow}(-\theta)} + 1}}, \quad (1.41)$$

where the double-subscript arrows denote the spin polarization direction during which a differential cross section is obtained. In this formula, instrumental efficiencies (and indeed all other factors, including neutron flux) are canceled in the ratios; this enabled the number of neutrons detected at a given angle to be substituted for the differential cross section.

1.6 Overview of Extant Data

Multiple measurements of the cross section and, separately, analyzing power have been made in the four (3+1)-nucleon elastic channels at energies comparable to those encountered here, with the notable exception of only the analyzing power for neutron-triton scattering. Table 1.1 catalogues these previous efforts for the systems other than $n-{}^3\text{He}$, which is covered by Table 1.2.

Of most direct relevance to the present study are the previous measurements of the $n-{}^3\text{He}$ analyzing power, with which there is some overlap in energy range.

Table 1.1: A catalogue of analyzing-power measurements for $p-3N$ and cross sections for $n-^3\text{H}$ elastic scattering at energies within a factor of two of any in the present work.

System	Observable	Energy (MeV)	Year	Reference
$p-^3\text{He}$	$A_y(\theta)$	$E_p = 1.00$	2006	B.M. Fisher <i>et al.</i>
		1.60	"	"
		2.25	"	"
		3.13	"	"
		4.05	"	"
	$A_{0y}(\theta)$	$E_p = 2.28$	2010	T. Daniels <i>et al.</i>
		2.77	"	"
		3.15	"	"
		4.02	"	"
		5.54	"	"
$p-^3\text{H}$	$A_y(\theta)$	$E_p = 4.15$	1976	R. Kankowsky <i>et al.</i>
		4.80	"	"
		6.35	"	"
		7.10	"	"
		9.90	"	"
$n-^3\text{H}$	$\sigma(\theta)$	$E_n = 1.0$	1960	J.D. Seagrave <i>et al.</i>
		2.0	"	"
		3.5	"	"
		6.0	"	"

Table 1.2: A catalogue of cross-section and analyzing-power measurements at energies within a factor of two of any in the present work.

System	Observable	Energy (MeV)	Year	Reference
n - ${}^3\text{He}$	σ	$E_n \in [1.5, 40.0]$	1983	Haesner <i>et al.</i>
		$\sigma(\theta)$	$E_n = 1.0$	1960
	2.0		"	"
	3.5		"	"
	6.0		"	"
	7.9		1974	L. Drigo <i>et al.</i>
	$A_y(\theta)$	0.94	1988	P. Jany <i>et al.</i>
		1.00	"	"
		1.05	"	"
		1.50	"	"
		1.67	1982	L. Drigo <i>et al.</i>
		2.00	1988	P. Jany <i>et al.</i>
		2.43	1982	L. Drigo <i>et al.</i>
		3.00	1972	C.E. Hollandsworth <i>et al.</i>
		3.00	1982	L. Drigo <i>et al.</i>
		3.4	"	"
		3.7	1985	H.O. Klages <i>et al.</i>
		7.4	1982	L. Drigo <i>et al.</i>
		8.0	1982	P.W. Lisowski <i>et al.</i>
	10.0	1985	H.O. Klages <i>et al.</i>	

2

Experimental Setup

2.1 Overview

The equipment involved in the measurement of the analyzing power of neutron- ^3He elastic scattering can be organized into three broad categories, each performing disparate functions: a polarized ion source, accelerator, and beam-transport elements (with which the source reaction targets and collimator for the neutron beam are most conveniently associated); targets and detectors; and signal-processing modules (hereafter “electronics”) and data acquisition. These are addressed in order below.

2.2 From Polarized Ion Production to Neutron Beam Production

2.2.1 Overview

Energetic polarized neutrons, needed for the analyzing power of interest to be measured, can be feasibly produced only in inelastic collisions of atomic nuclei (as free neutrons neither exist in significant numbers, due to a macroscopically short half-life, nor can be practically accelerated laterally). Polarization can be achieved either by selecting a scattering angle, for unpolarized ions, at which the produced neutrons

have a nonzero polarization, or from polarized ions (for which the produced neutrons generally have nonzero polarization). For this experiment, we used the latter method, requiring a source of polarized ions—in our case, protons and deuterons—as well as a target for neutron production (as opposed to the target of interest to the experiment, ^3He). This section describes these as well as the beam transport between source and target.

2.2.2 Ion Source

The source for polarized hydrogen nuclei, the protons and deuterons used for neutron production, was TUNL’s Atomic Beam Polarized Ion Source (ABPIS), a diagram of which is presented in Fig. 2.1. As hydrogen is molecular under terrestrial conditions (most pertinently storage at room temperature), for the method of polarization and acceleration employed, it is necessary first to dissociate the hydrogen molecules into the constituent atoms. This is achieved by exposing the gas entering ABPIS to a radio-frequency (RF) discharge. The resulting atomic hydrogen is propelled by overpressure through a cryogenic nozzle, which is kept cooled and coated with nitrogen to inhibit molecular recombination of the hydrogen. This also effectively serves to collimate the neutral atomic beam in the direction of the remaining elements of the source (of importance, as until the beam becomes ionized, acceleration is unfeasible), as does the beam’s subsequent passage through a narrow aperture (“skimmer”). The beam then enters the spin-selection region of the ABPIS, in which a preferential direction for the nuclear spin is established.

In order to polarize the hydrogen nuclei, as needed for our utilized method of polarized neutron production, a state of specific electron and nuclear spins is preferentially populated. The role of electron spin here is important, as the relevant atomic energy levels of either protium or deuterium in a strong magnetic field are dominated by the interaction of the electron with the magnetic field; such a magnetic field is ultimately needed to define the direction of polarization. There are two degenerate energy levels for the $l = 0$ (i.e., s in spectroscopic notation) atomic states of hydrogen in the absence of external fields, due to hyperfine splitting, distinguishing states of different total spin j : 0 and \hbar for protium, $\hbar/2$ and $3\hbar/2$ in the case of deuterium. This degeneracy is lifted in the presence of an external magnetic field, as shown in Fig. 2.2, the Breit-Rabi diagram for protium, and Fig. 2.3, that for deuterium: in the high-field limit, the energy levels (and hence the corresponding eigenstates) are states of definite electron and nuclear spin, instead of total spin. This enables the selection of a particular nuclear state through the selection of an electron spin state and subsequent RF pumping.

However, for the RF transitions between these levels to have an effect on the nuclear polarization of the beam, it is first necessary to depopulate some states (otherwise, the balance between absorption and stimulated emission would maintain an effectively equal population of all states). To this end, a magnetic sextupole was used as a Stern-Gerlach filter on the beam emerging from the skimmer to select only the electron spins in the direction of the local field; atoms thus selected were focused by the sextupole, while rejected atoms were defocused away. While the beam at this stage lacked a common polarization axis, a smooth transition to a region with a strong, uniform field largely retained polarization while providing the common axis.¹

¹ The conditions for the polarization retention are that the Larmor precession frequency be sufficiently high that changes in the magnetic field are adiabatic with respect to the particle's passage, and that no zero-field regions are encountered. These are not met for all trajectories through this part of the source, and so there is some loss of polarization at this stage.

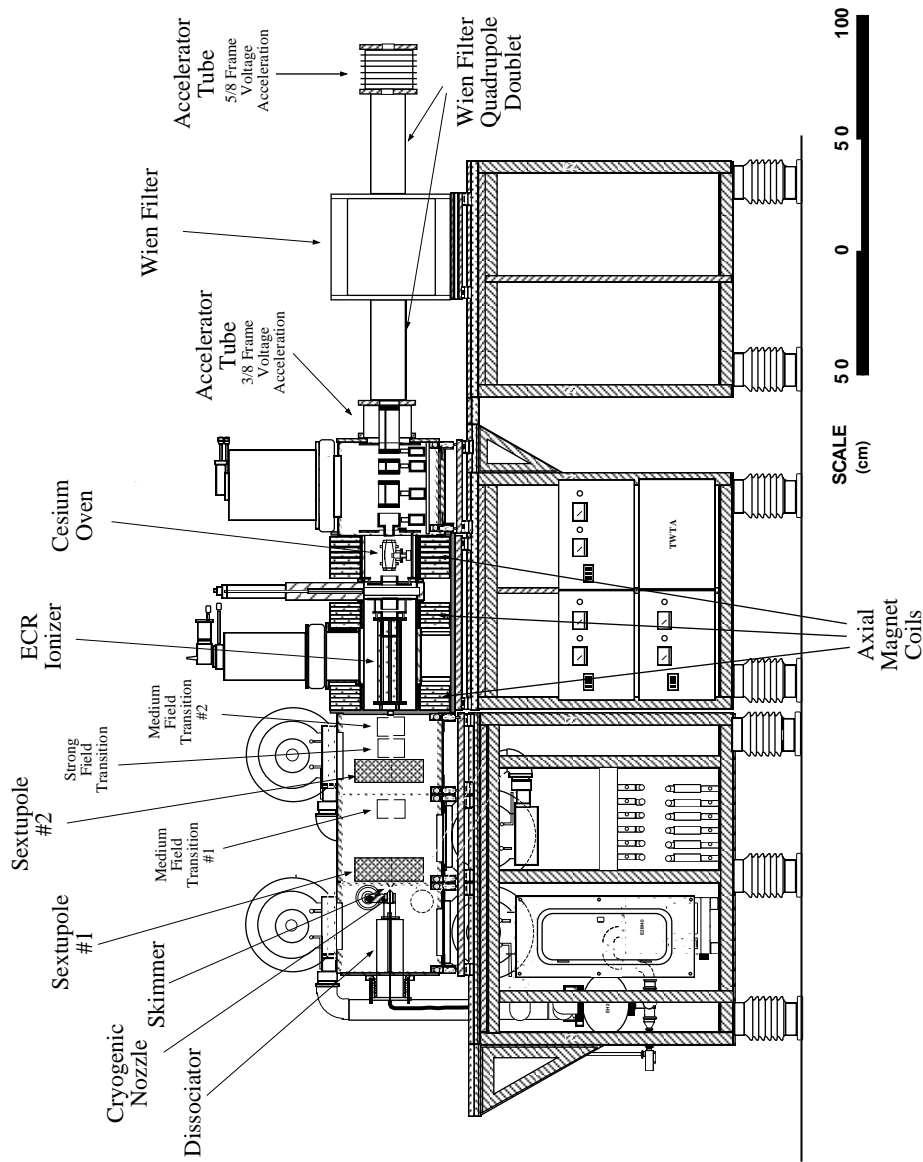


FIGURE 2.1: A diagram of TUNL's Atomic Beam Polarized Ion Source (ABPIS). Hydrogen is provided to the dissociator through a pipe represented here by a dark curve immediately to the left of the dissociator's axis.

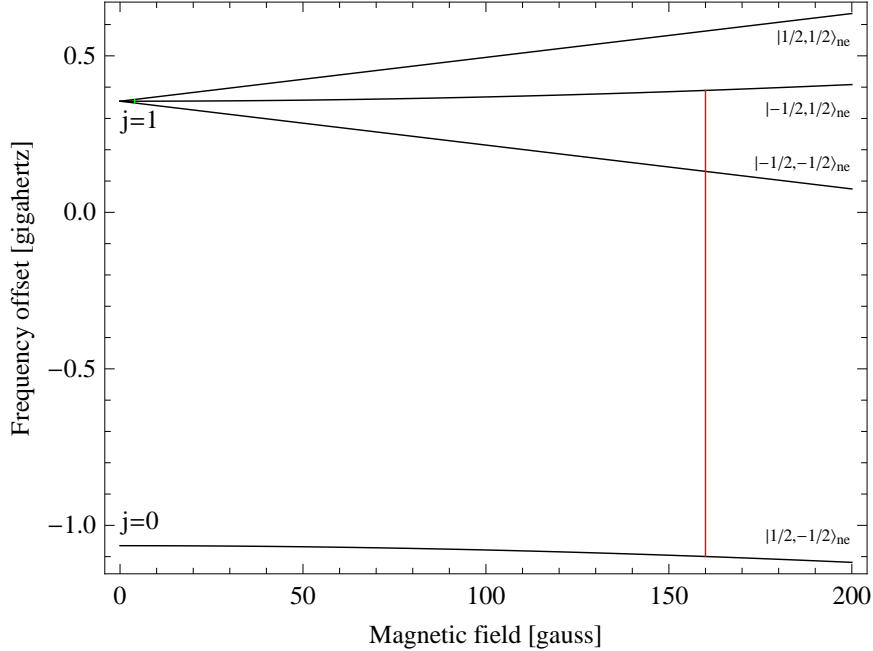


FIGURE 2.2: The Breit-Rabi diagram for protium, showing the frequency difference from a hypothetical baseline where hyperfine and Zeeman contributions to the energy have been omitted. Labels for the states at 200 gauss are incorrect, though as intended—consisting of the spin projections in units of \hbar along the magnetic field of the nucleus (the proton in this instance) and the electron, respectively—and are used to represent the high-field limit associated with each energy eigenvalue; labels for zero field, for j (the total spin) in units of \hbar , are exact. The RF transitions used are shown in color (medium-field in green, strong-field in red; see Table 2.1).

The ABPIS employs three RF transition units (designated, according to magnetic field strength, medium-field-1, medium-field-2, and strong-field—MF1, MF2, and SF, respectively, though the last two are encountered in reverse order) in addition to a sextupole other than the one just mentioned (located between the MF1 and SF transition units) to enable rapid switching between states as well as the selection of polarization states beyond the ones used for this experiment (the tensor polarization of the deuteron). For vector polarization, only two of these RF units were in use, namely, SF and MF2. For both isotopes, a strong-field transition inverts nuclear spins antiparallel to the field, thus creating a beam with net positive polarization. The medium-field transition similarly inverts nuclear spins parallel to the field for protium

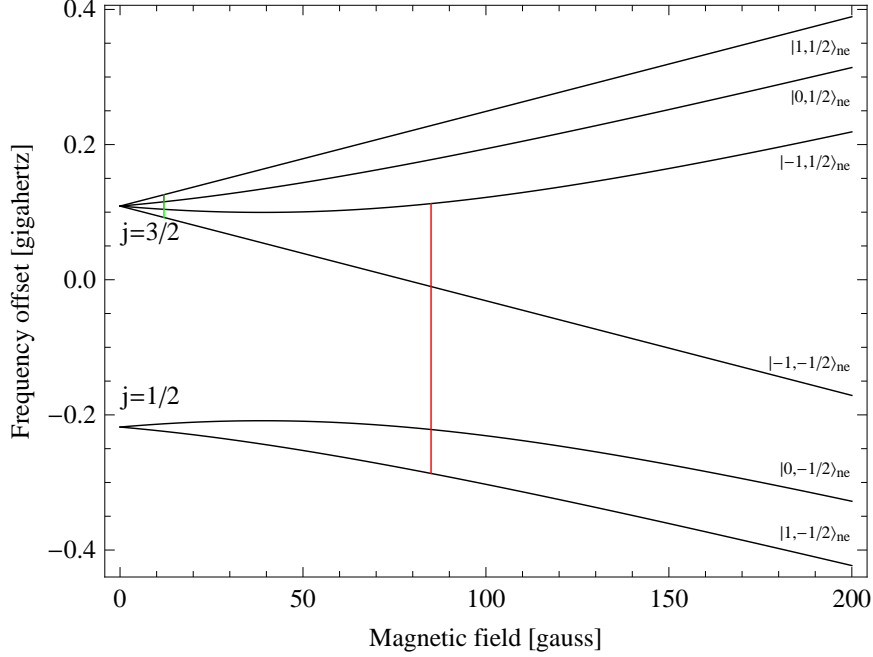


FIGURE 2.3: The Breit-Rabi diagram for deuterium, again with hypothetical hyperfine-free frequency baseline; labels of states and their exactness are as in Fig. 2.2; transitions have again been highlighted in color, with the simultaneous medium-field transitions unique in this experiment to deuterium shown in varying hues of green.

to produce negatively polarized beam; for deuterium, optimal beam production relies on simultaneous transitions between the four states approximating $j = 3\hbar/2$ due to the roughly equal spacing of those levels at low magnetic field strength, with the net effect again being the conversion of nuclear spin parallel to the field to that antiparallel (and again a negatively polarized beam).

Table 2.1: RF transition units settings for production of the various spin states used for neutron production.

Atom	Desired State	SF		MF2	
		$ \mathbf{B} $ (g)	f (MHz)	$ \mathbf{B} $ (g)	f (MHz)
D^0	\uparrow	85	400	off	
D^0	\downarrow	off		12	12
H^0	\uparrow	160	1485	off	
H^0	\downarrow	off		4	12

With the desired nuclear spin states thus selected, it remains to accelerate the beam to the desired energy and towards the target. This is achieved first by ionizing the atomic beam, which occurs in an electron cyclotron resonance (ECR) ionizer due to electrons driven at resonance in a strong solenoidal magnetic field colliding with the atoms in the beam. The resulting hydrogen nuclei are then accelerated towards a cesium oven, where the high electropositivity of the cesium vapor contained therein results in a significant fraction (~ 0.2) of the beam becoming negatively charged.² Before leaving the ABPIS, the beam passes through a magnetic quadrupole doublet and Wien filter, the latter of which was used to rotate the beam polarization axis to its desired direction. (Compensation for subsequent precession in magnetic elements of the beam transport system was not needed in our case, as the polarization axis and the fields of the inflection magnets were parallel.)

2.2.3 Beam Transport

The polarized hydrogen ions emerge from the polarized source with insufficient energy to produce the desired neutron beam; furthermore, the location of the experimental hall in TUNL required nontrivial beam transport. At the most basic, given the energy requirements of this experiment and the existing geometry of TUNL, two inflection magnets and the accelerator were needed: the first inflection magnet deflected the negative ion beam exiting the polarized source by 30° to align with the low energy beam pipe; the second, located in proximity to and after the accelerator, deflected the fully accelerated beam, now nuclear, by 38° to align with the beam pipe leading to the Neutron Time-of-Flight hall, in which the reaction of interest occurred. The accelerator was a FN tandem Van de Graaff manufactured by High Voltage Engineering, and capable of generating a positive terminal voltage of 10 MV.

The needs of focusing and more sensitive steering of the beam, however, required

² As with all non-noble elements, a neutral hydrogen atom can accept an extra electron.

a variety of other beam elements. As Fig. 2.4 shows, these included two low-energy electrostatic quadrupoles, a total of twelve (eleven functioning) magnetic dipole steerers, an Einzel lens, a pair on either side of the accelerator (and three pairs on the 38° beam pipe) of focusing magnetic quadrupoles, and a gridded electrostatic lens within the accelerator. Adjustable horizontal and vertical blinds, referred to as slits, within the beam pipe between the accelerator and the second inflection magnet enabled further constraints on the beam profile as well as, in the case of the horizontal slits³ in conjunction with the latter inflection magnet, control of the energy spread. A further set of similar slits, on which the charge deposited by the beam was obtained, were used in feedback with the accelerator to stabilize terminal voltage fluctuations: under ideal conditions (notably a correct terminal potential, and properly adjusted slits), the beam is equidistant from the slits and deposits commensurate charges on either slit; a higher terminal voltage would then lead to a larger radius of curvature through the second inflection magnet and hence more charge on the slit nearer the original trajectory emanating from the tandem; a lower terminal voltage likewise would result in more charge on the slit further from the undeflected trajectory.

³ That is, constraining the beam in the horizontal direction; the blinds themselves define a vertically extended slit.

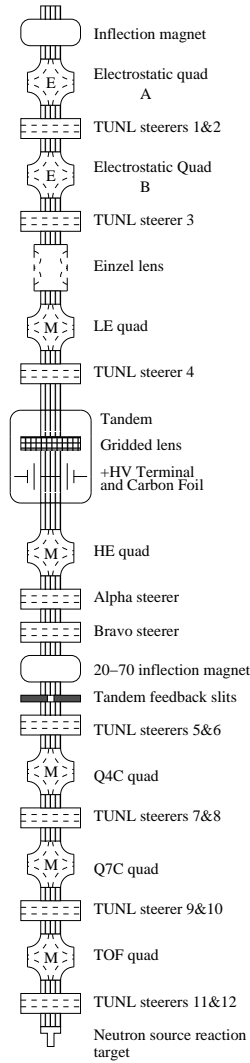


FIGURE 2.4: Schematic diagram of the beamline components involved in the transmission of the primary beams used in neutron production.

2.2.4 Accelerator

The principle behind the tandem accelerator is that of using the high positive terminal voltage to attract an incoming negative ion, then, after reversing the charge of the ion, to repel it, thus increasing the particle's energy by twice the terminal voltage times the electron charge. The charge exchange is achieved by the placement

of a carbon foil near the terminal, which has a high probability⁴ of stripping two electrons from the incoming negative ions.

2.2.5 Neutron Beam Production

At the end of beam pipe in the Neutron Time-of-Flight hall, the polarized hydrogen nuclei collided with one of two targets; the choice of which, in conjunction with that of the incident isotope of hydrogen, depended on the desired neutron energy. The reactions used were ${}^2\text{H}(\vec{d}, \vec{n}){}^3\text{He}$, with a Q-value of 3.268 MeV, and ${}^3\text{H}(\vec{p}, \vec{n}){}^3\text{He}$, with Q-value -764 keV. The Q-value constrained the former interaction, for which the target was the deuterium gas cell displayed in Fig. 2.5, to be employed only for the production of 4.05 and 5.54 MeV neutrons, where it was favored over the latter, whose target was instead a tritiated titanium foil with significantly less reactant (3 Ci implanted in 2.2 mg/cm² titanium, itself evaporated onto a .4 mm molybdenum backing) pictured in Fig. 2.6. The polarization transfer coefficients were 0.41 and 0.58 (as determined in [Rop10]) at 4.05 and 5.54 MeV, respectively.

As energy loss was substantial in both targets, due to passage through foils and spatially extended reactant, beam energies were chosen to produce neutrons of the desired energy in the centers of the deuterium gas and titanium foil. These losses additionally provided an accurate estimate of the energy spread of the resulting neutron beam, with the spread being estimated by the loss in traversing half of the source reactant (deuterium gas or the tritiated titanium) added in quadrature to 10% of the loss in preceding elements (Havar foil, and helium buffer for the tritiated target). These spreads, as well as other operating parameters, are detailed for the deuterium gas cell in Table 2.2, and for the tritiated titanium target in Table 2.3.

⁴ See, for instance, the equilibrium charge states presented in [Mar68], p. 36.

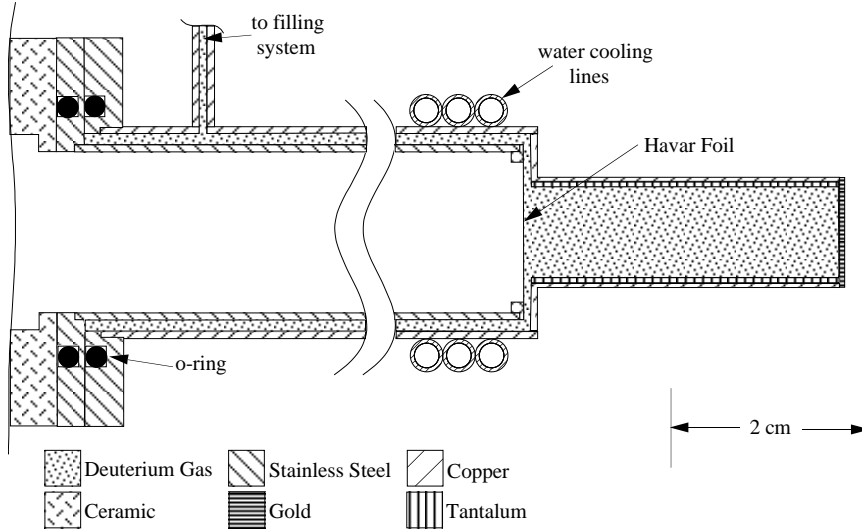


FIGURE 2.5: A cell (figure from [Bra98]) very similar to that used as the deuterium gas target in the present experiment for the production of 4.05 and 5.54 MeV neutrons; as gas cooling was employed, the water cooling lines were absent.

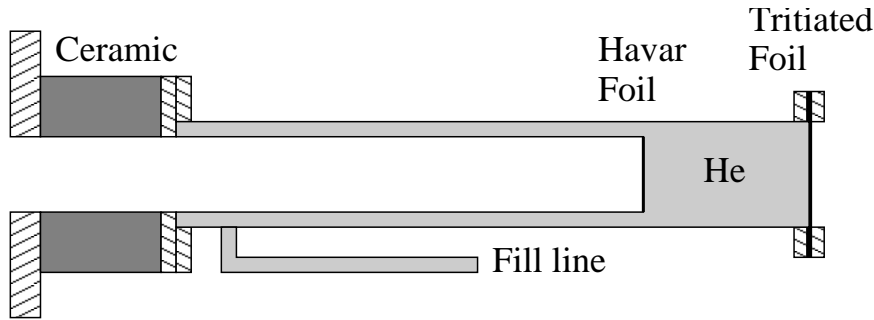


FIGURE 2.6: The cell containing the titanium foil impregnated with tritium used to generate neutrons with energies between 1.60 and 3.14 MeV; the total length of the cell is 13 cm.

2.3 Targets and Detectors

2.3.1 Overview

We intentionally exposed two targets to the neutron beam as defined by the polyethylene collimator: a gas scintillator containing enriched ^3He , and a gas scintillator containing natural helium. The former was necessary to obtain the analyzing power of interest, that of elastic neutron- ^3He scattering; the latter, with the preponderance of

Table 2.2: Pressures of the deuterium gas cell, the required beam energies to obtain a central energy corresponding directly to that of the produced neutrons, and resulting neutron energy spread, for neutron production at 4.05 and 5.54 MeV. All energies in the table are in MeV; the pressures are in atmospheres.

E_n	P_d	E_d^{Beamline}	$E_d^{\text{Cell center}}$	$\Delta_{E_n}^{\text{FWHM}}$
4.05	1.0	1.90	0.93	0.34
5.54	2.0	3.04	2.29	0.33

Table 2.3: Energy losses and resulting spreads for neutron production via the p - ^3H reaction at 1.60, 2.26 and 3.14 MeV. All energies are once again in MeV.

E_n	E_p^{Beamline}	$E_p^{\text{Ti center}}$	$\Delta_{E_n}^{\text{FWHM}}$
1.60	2.70	2.39	0.17
2.26	3.30	3.04	0.13
3.14	4.15	3.92	0.11

^4He in natural helium and the well-determined and, for an appropriate choice of angle, large analyzing power of neutron- ^4He elastic scattering at the energies involved in this experiment, sufficed for an accurate determination of the neutron polarization. Surrounding either scattering target was an array, in the horizontal plane of and symmetric with respect to the path of the beam, of liquid scintillator neutron detectors. To reduce the overall duration of the experiment without sacrificing precision or angular resolution, four pairs of neutron detectors were operated simultaneously at distinct angles about the ^3He target; as only one angle was needed for the determination of polarization via the neutron- ^4He analyzing power, only one pair of neutron detectors was deployed about the ^4He target. These configurations, as well as their positions relative to the gas cell of the neutron source reaction and the polyethylene collimator, are shown in Fig. 2.7.

2.3.2 ^3He Gas Scintillator

The ^3He gas scintillator used in these measurements was designed and constructed at TUNL, with the present measurement as motivation (in conjunction with γ - ^3He reactions). The design, shown in Fig. 2.8, consisted of a 1-mm-thick stainless steel

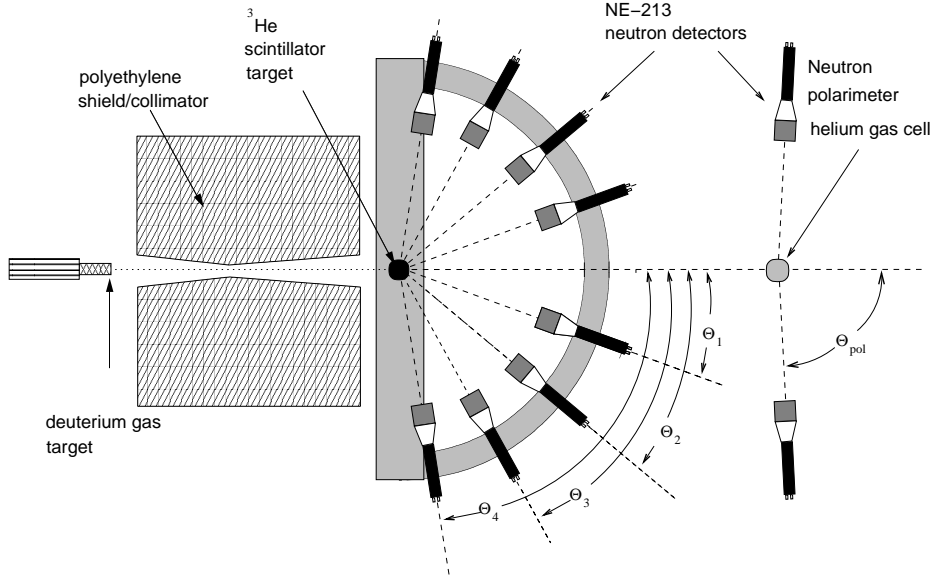


FIGURE 2.7: Diagram of detectors and their positions relative to the neutron source reaction for a measurement at $\theta_{lab} \leq \pi/2$; while not to scale, the positions are closely approximated. The beam pipe is represented by the segment at far left, with the target for the source reaction mounted at the end of the pipe. The typical center-to-center distance between the source-reaction target and the ^3He gas scintillator was 86 cm; that between the ^3He gas scintillator and the surrounding neutron detectors was 48 cm. For measurements at $\theta_{lab} > \pi/2$, the semicircular ring supporting the primary array was rotated in the plane by π about the midpoint of the horizontal radius of the semicircle.

cylindrical shell 11 cm long with a 26.5-mm inner radius with one base replaced by a hemisphere of equal radius and centered on the axis, the other base absent and surrounded by a flange; covering this opening at the base of the cylinder was a 1-cm-thick Pyrex glass window. The shared boundary of the glass and the lower part of the flange was beveled so that interior overpressure could not displace the glass, which was further affixed to the flange with a two-component glue. Adjacent to the flange on the cylinder was a 3/16" hole to allow for filling and evacuation via a steel tube hard-soldered to the cylinder. The inner surface of the stainless steel was coated with MgO, the high reflectivity of which enhanced light collection from scintillation; this and the inner surface of the glass window were subsequently

coated w
 ultraviol
 exterior s
 in electri

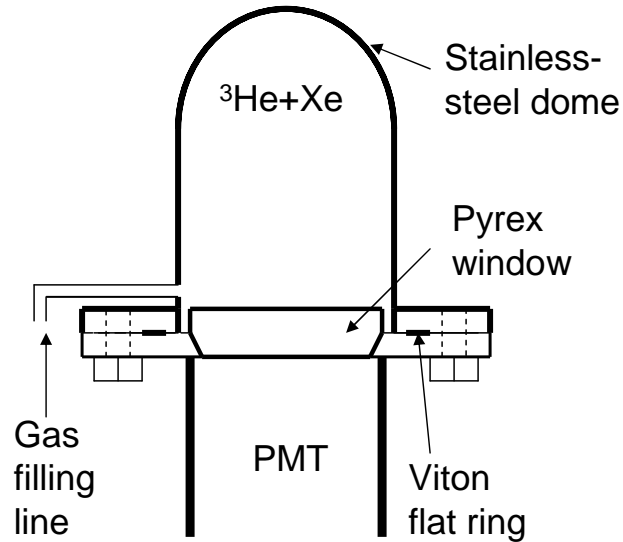


FIGURE 2.8: The design of the ^3He cell used as scatterer and, as an active target in conjunction with a photomultiplier tube, center detector in the primary array.

For the purpose of this experiment, the gas cells were filled with high-grade ^3He with an admixture of xenon that provided, as determined from a characterization study undertaken in 2005 (see [Tor11]), a satisfactory combination of light output and insensitivity to electrons produced within the gas (which would correspond to γ -induced events, in which there was no interest). The combination used at the outset consisted of 52.5 atm ^3He and 2.5 atm Xe.

2.3.3 ^4He Gas Scintillator

The ^4He scintillator (which was, by contrast, a preexisting apparatus designed and constructed at Eberhard Karls Universität Tübingen) consisted of a steel cylindrical surface terminating in two flanges each fitted with a Pyrex glass window in the

manner described for the ^3He scintillator; to each window a photomultiplier tube was affixed, as shown in Fig. 2.9. The gas used was a mixture of 93% natural helium (overwhelmingly ^4He) and 7% xenon, by pressure, which totaled 68 atm.

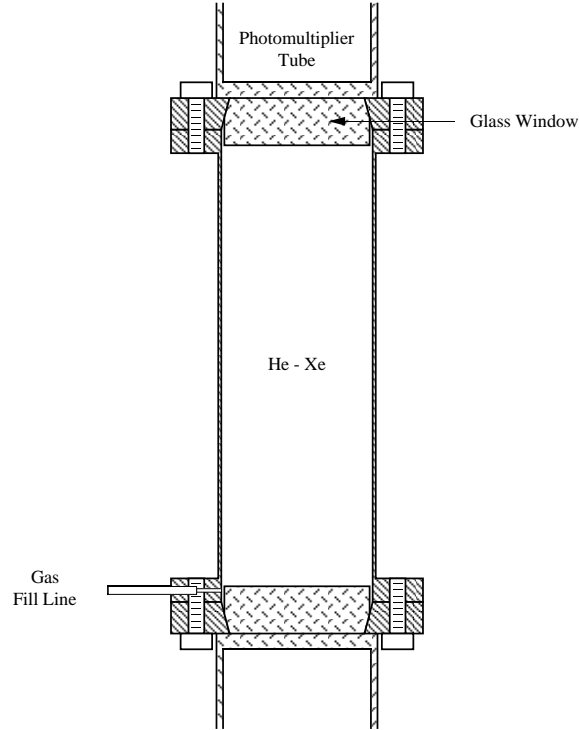


FIGURE 2.9: The design of the ^4He cell used as scatterer and center detector in the polarimeter array.

2.3.4 Neutron detectors

The neutron detectors, designed and developed at TUNL, contained the liquid hydrocarbon scintillator NE213 in a rectangular prism whose active volume was 11.86 cm high, 4.26 cm wide, and 7.52 cm deep. To one of the narrow vertical faces of this prism a tapered acrylic light guide to a photomultiplier tube was attached; the remaining faces were covered by a 1-mm-thick layer of aluminum.

As with the He-Xe gas mixtures used in the aforementioned active targets, the scintillating liquid used here produced signals in response to both neutron- and γ -

induced events (nuclear and electron recoils, respectively); in contrast to those produced in the scintillating gas, however, the signals associated with neutrons and γ 's had distinguishable time dependences. Both signals were characterized by, following an abrupt displacement from the baseline, a superposition of exponential decays with a common set of decay constants:⁵ the coefficient (relative to the signal maximum) of the slowest-decaying term is larger in neutron-induced events than in γ -induced events.

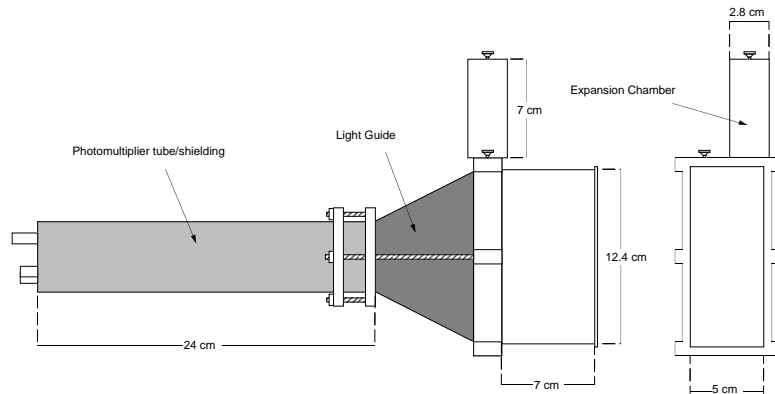


FIGURE 2.10: The design of the neutron detectors used in the primary and polarimeter arrays. This model was developed and built at TUNL, hence the absence of an industry reference.

⁵ See, for instance, [Mar02], in which the decay time constants attributable to the NE213 scintillator fluid were found to be around 5 and 35 ns.

3.1 Overview

The signals from the detectors in these arrays, being analog, are not themselves feasibly storeable with available methods; furthermore, the time differences between physically correlated signals is of critical importance to this measurement. For these reasons, several signal processing modules were employed. While we were concerned only with correlations between signals from each neutron detector and the active target in its array, not between those from different neutron detectors (or between arrays), there were not enough modules to build independent electronics for each such coincidence: instead, we had only two independent electronic configurations, one for each array. These are described in more detail in the following subsections.

In addition to quantitative data, signals directing their acquisition into memory—“triggers”—were generated by these electronics; as the electronics primarily associated with the generation of the triggers were quite substantial, they will be given distinct attention. The software responsible for data acquisition (DAQ) and the interface with the electronics will also be addressed.

Finally, as spin-state control for the polarized source was partially incorporated

into these designs, the configuration for that is described here as well.

3.1.1 Description of Quantities of Interest

In the idealized absence of background, the number of signals received from each neutron detector (which would then correspond, with an ultimately negligible factor of efficiency,¹ to the number of neutrons scattered into that detector) in a given polarization state could be directly entered into the formula for the analyzing power. In reality, contamination from γ 's inevitably produced in stopping the ion beams from the tandem, in addition to the detection of neutrons scattered from "targets" other than the ^3He cell, makes this unfeasible. It is therefore desired to have some form of particle identification associated with every such signal. This is achieved in two ways: through pulse-shape discrimination (PSD), which analyzes the time dependence of individual signals, and, utilizing the detection capabilities of the target, through the calculation of time elapsed between scattering and detection. Involving the gas cell as a "center detector" introduces a problem particular to n - ^3He scattering, namely contamination from the $^3\text{He}(n,p)^3\text{H}$ reaction (which, being exothermic with a Q-value of 764 keV, renders the center detector sensitive to slow neutrons, which are otherwise undetectable), and necessitates the accounting of the total energy associated with each center detector signal. Though not as clearly motivated, the energies associated with recoils in the ^4He cell and neutron detectors are also useful in particle identification and thus recorded.

3.2 Description of Implementation

3.2.1 Common Elements

Due to the common quantities of interest (particularly for the neutron detectors), several electronics modules were utilized in both configurations, which are glossed

¹ Note the cancellation of efficiencies, though inexact in realistic conditions, in the formula for the analyzing power.

below. PSD modules (Canberra 2160 in both designs) received the neutron detector signals first, and provided as output a logic pulse delayed by a length corresponding to an effective decay time (as determined by the combinations of decay times given in §2.3), providing distinct timing distributions for neutron- and γ -induced events. Constant-fraction discriminators had an amplitude-independent response time to incoming pulses and therefore were used to obtain a timing signal that was sufficiently accurate to determine flight-times to within a few nanoseconds.² Integrated signal amplitudes were obtained, subsequent to amplification, by analog-to-digital converters (ADC's), with Ortec 413 and Silena 4418 being the models used. Both flight-times and PSD signals (as, once again, the latter are generated as logic signals with a pulse-shape-dependent delay) are processed by similar timing modules, the choice of which differing between arrays: for the primary, a time-to-digital converter (TDC, specifically a Phillips 7186) was used; for the polarimeter, a combination of time-to-amplitude converters (TAC's; here Ortec 567) and ADC's were employed.

The triggers functioned not only to prompt data acquisition but also to provide a “start” signal to timing digitizers,³; for both, consideration must be taken to avoid superfluous, and potentially lossy, triggering. To that end, to limit the primary array trigger to only events that involved center-side coincidences (and, more generally, to generate a common trigger for either array), multiple Philips 755 logic modules were employed, at various coincidence levels (hence functioning as logical conjunctions and disjunctions). Finally, logic signals had to conform to, and in some cases be translated between, either Nuclear Instrumentation Module (NIM) or Emitter-Coupled Logic (ECL) standard.

A final shared aspect of both trigger designs are the veto signals, which are set

² Typical FWHM in analyzed spectra around 60 channels, at .2 ns/channel (therefore 12 ns).

³ The triggers so generated are required essentially for any digitizer: for the ADC's, this was in the form of a logic gate.

in anticoincidence with the center-side coincidences mentioned above (which form an “incipient trigger,” as it will be called hereafter) in order to prevent overwriting of channels during the read-out of digitizers or the reading of buffers during data acquisition. These vetoes for both arrays consist of a logical disjunction of four elements: an inhibit signal from the spin state electronics during spin flips, another generated by the trigger supervisor during data acquisition, a third from a gate and delay generator (preventing multiple triggering of the digitizers), and the complement of a “beam window” gate. The last of these was meant to exclude necessarily extraneous signals obtained during a temporary mistuning of the beam (most often due to an uncontrolled fluctuation in the characteristics of the beam, most often due to transient malfunctions in the ion source) by generating a gate while the beam current was between two manually set limits; for portions of the experiment, this was unintentionally disabled, though the effect was small.

Lastly, and of only indirect importance to the analysis, scaler modules (in our case, a set of 24-bit integer registers which increment with each received trigger signal) was used to record the number of signals obtained from each detector, as well as center-side coincidences both vetoed and un-vetoed: no data reduction could be applied to these values as they were read out only at the conclusion of a run, and hence not in meaningful conjunction with any other quantities⁴. However, as these data functioned diagnostically during the experiment, the inputs to the scaler modules are explicitly noted in the following descriptions.

3.2.2 Spin-State and Beam-Current Electronics

The spin-flip desired for convenient detector efficiency cancellation was configured, incorporated into both trigger structures (due to the necessity of excluding a period

⁴ Making them somewhat like their mathematical homonyms, as invariants under any subsequent operations; regardless, the nomenclatures remain distinct.

of poorly-determined and otherwise low polarization during transitions between spin states), and made available in the form of “spin-up” and “spin-down” logic gates to data acquisition by the design presented in Fig. 3.1.

Although beam current was primarily diagnostic (and a gauge on the beam-current integrator displayed the beam current in real time), a digitized record was nonetheless desirable to consult, particularly in conjunction with the spin state; for this purpose, a logic signal from the beam-current integrator was sent, to separate scaler modules, directly as well as in logical conjunction with the spin-up and spin-down signals.

3.2.3 Primary array electronics

The electronics used for the primary array are graphically presented in block diagram form in Fig. 3.2, with the trigger electronics excised to form Fig. 3.3.

As mentioned in §3.2.1, a Philips 7186 TDC was employed in this design; this was due to the large number of independent timing determinations (each side detector being associated with two, for both PSD and center-side flight-time), which exceeded the available supply of TAC’s and ADC’s. This TDC had sixteen input channels for which a time difference could be obtained from a common “start” or “stop” signal; we used the former in the form of a logical disjunction of all center-side coincidences. Thus, while “stop” signals were received by this single module from all side detectors, each corresponded to a distinct output.

Signals from any given side detector were fanned three ways: into an amplifier, the output of which was subsequently digitized by the Silena ADC; into a PSD module, output subsequently being received as a “stop” signal by the TDC; and into a CFD. The fanned output of that CFD essentially served four distinct functions: one triggered (or “strobed,” in common parlance) the PSD module, another was taken in coincidence with the center detector CFD and thereafter taken in logical

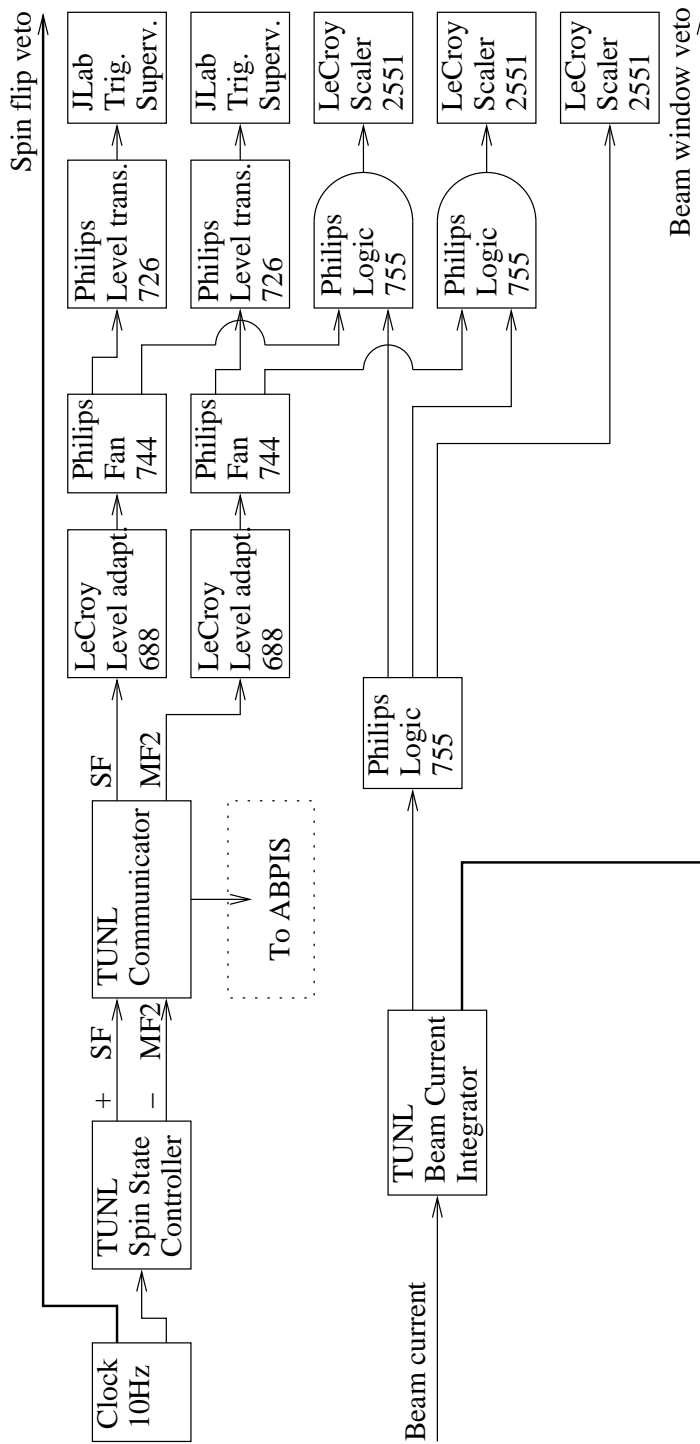


FIGURE 3.1: Block diagram of the electronics for the spin state electronics.

disjunction with all other such center-side coincidences to form the incipient primary array trigger, and, subsequent to lengthening via a Philips discriminator unit, a third provided both a “stop” signal to the TDC and incremented a LeCroy scaler unit.

Signals from the center detector, not being subject to PSD, were fanned two ways, into an amplifier (and thereafter an Ortec 413 ADC) and into a CFD; the output of the latter was taken in coincidence with the various side detector CFD signals in the generation of the trigger, and also incremented a LeCroy scaler unit.

To form the trigger, the incipient trigger must be taken in anticoincidence with the various vetoes, although it is first fanned to two scalers (directly to one, in disjunction with the incipient polarimeter trigger for the other) in addition to the logic unit providing the anticoincidence. The resulting vetoed trigger served as a start signal for the TDC; through a gate and delay generator, provided the gate for the Silena and Ortec ADC’s; and finally prompted data acquisition as an input to the JLab trigger supervisor module.

3.2.4 Polarimeter Electronics

The block diagram and trigger detail for the polarimeter array are presented in Figs. 3.4 and 3.5, respectively.

The main difference between the treatment of the polarimeter and the primary array as regards electronics is the use of TAC’s (and subsequent digitization by ADC’s) in place of the TDC; the greater freedom in the choice of “start” and “stop” signals this afforded did result in a different standard for several quantities, however. Thus, while the side detector signals were again initially sent separately to amplifier, PSD module, and CFD, an output of the CFD was used (via a time pickoff) to trigger a TAC which received the PSD output as a “stop” signal. This avoided the flight-time offset present in the primary array PSD values. The other outputs of the CFD were used again to strobe the PSD module, generate a trigger via a three-

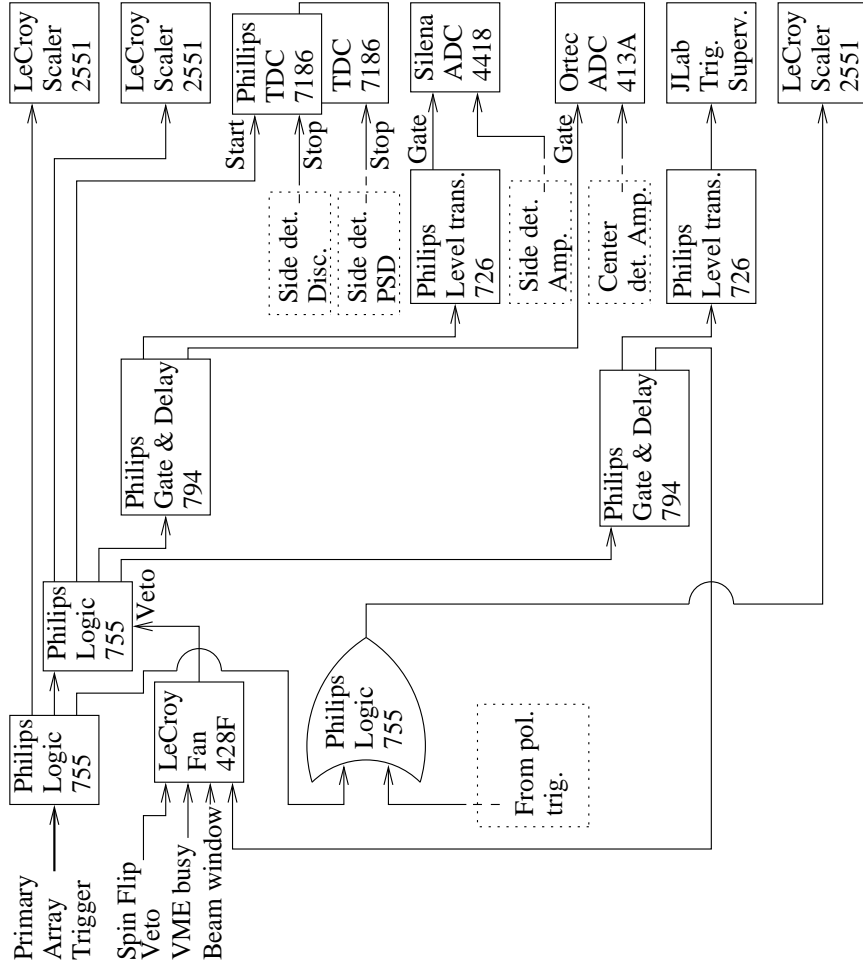


FIGURE 3.3: Detail of the electronics for the primary array trigger. The TDC here doubled corresponds to the distinct elements for PSD and flight-time as presented in the preceding figure; in reality, only one TDC module was employed. While it is not shown here to avoid cluttering, the VME busy signal is a product of the JLab trigger supervisor module.

way coincidence with the PSD and flight-time outputs and subsequent disjunction with a like coincidence for the other side detector (and repeated use of gate and delay generators to ensure proper duration and timing), and, through the pickoff, trigger the flight-time TAC (in addition to the PSD module already mentioned) and increment a LeCroy scaler unit. As the “stop” signal for the flight-time TAC came from the delayed ^4He cell CFD, obtained times were inverted with respect to actual flight-times (this being in contrast to the primary array, where a coincidence between center and side detectors provided the trigger, and the side detector the “stop,” resulting in regular orientation).

The polarimeter trigger was formed in much the same way as in the primary array; not being needed for a TDC, it nonetheless likewise contributed to scalers, generated the gate for the ADC, and prompted data acquisition through the trigger supervisor.

3.3 Trigger Supervision and Data Acquisition

Upon receiving a trigger from either array’s electronics, the trigger supervisor module commenced a read-out of the digitizers, and generated a “VME busy” veto signal with a duration of approximately 200 ns; this was the time needed to prevent interference from incoming signals while modules were being read out. CEBAF Online Data Acquisition (CODA) software was used to acquire these read-outs and format them for storage and processing on Linux workstations.

Experimental Synopsis

4.1 Overview

Data was collected during a combined 1568 hours¹ of measurement into a total of 1239 runs intermittently over the course of more than two years, from June 2004 to November 2006. Among these runs are 68 contiguous² sets with identical neutron energy, detector geometry, and settings (both of detectors, e.g. voltage, and control-room electronics), enabling analysis of each set with consistent values of parameters (of which more will be detailed in Chapter 5).

4.2 Summary of Data

Tables 4.1 and 4.2 provide a comprehensive account of runs for which the analyzing power was determined with adequate accuracy, organized according to the linux workstation employed in data acquisition (two machines designated “DAQ2” and “DAQ4”); a further 24 runs, taken with DAQ4 and numbered 720 - 734 and 766 - 774, were excluded from analysis due to uniformly low neutron polarization (measured to

¹ Equivalent to 65 days and eight hours.

² Rather, very nearly so; each set constituted an interval among run numbers with usable data.

be significantly less than .2 in every such run).³

Since, for a particular neutron energy, the analyzing power at a specific pair of scattering angles is often measured over the course of more than one run group (with the distinction of run groups in certain cases being only for the ease of analysis), a more direct presentation of the exposure for each energy-angle pair is given in Table 4.4 .

³ While durations and event totals provide an adequate synopsis of the measurement, they provide only a very rough estimate of signal accumulation. In particular, among the enumerated events were those due to photons or accidental center-side coincidences, identifiable only in subsequent analysis, which could be extremely sensitive to threshold settings: for instance, while DAQ4 runs 423-437 had over four times the events of runs 438-446 on the same machine, their numbers of neutrons of interest were nearly the same. The duration of run groups can likewise be misleading, being dependent on a value of beam current to get the more relevant quantity, fluence (an estimate of which was obtained during operation from the TUNL BCI, but these values were highly prone to error and lack a reliable record).

Table 4.1: A list of the 622 runs for which usable data was acquired while using the DAQ4 workstation (this omits the 24 runs that were recorded, but excluded from analysis due to low neutron polarization). Superscripts indicate missing runs detailed in Table 4.3.

E_n^{lab}	θ_1^{lab}	θ_2^{lab}	θ_3^{lab}	θ_4^{lab}	Run nos.	Duration	Events
5.54	30°	50°	70°	90°	122 - 149 ¹	30 h	1.47×10^6
5.54	25°	40°	60°	80°	151 - 170	19 h	2.03×10^6
5.54	28°	45°	65°	85°	171 - 185 ²	12 h	1.08×10^6
5.54	20°	35°	55°	75°	186 - 194	10 h	$.55 \times 10^6$
5.54	20°	35°	55°	75°	201 - 206	6 h	$.45 \times 10^6$
4.05	30°	50°	70°	90°	212 - 259	53 h	$.65 \times 10^6$
4.05	20°	40°	60°	80°	281 - 298	21 h	$.38 \times 10^6$
4.05	25°	45°	65°	85°	300 - 326	30 h	$.41 \times 10^6$
4.05	35°	55°	75°	90°	330 - 355	34 h	$.39 \times 10^6$
4.05	35°	55°	75°	90°	358 - 368	12 h	$.32 \times 10^6$
4.05	30°	50°	70°	85°	369 - 390	25 h	$.60 \times 10^6$
4.05	20°	45°	65°	80°	391 - 404	16 h	$.40 \times 10^6$
4.05	20°	40°	60°	80°	406 - 418	15 h	$.41 \times 10^6$
5.54	95°	110°	125°	140°	423 - 437	15 h	1.11×10^6
5.54	95°	110°	125°	140°	438 - 446	12 h	$.23 \times 10^6$
5.54	100°	115°	130°	145°	447 - 467	22 h	$.50 \times 10^6$
5.54	105°	120°	135°	150°	468 - 482	14 h	$.39 \times 10^6$
5.54	105°	120°	135°	90°	483 - 490	8 h	$.18 \times 10^6$
4.05	95°	110°	125°	140°	493 - 503	14 h	$.07 \times 10^6$
4.05	95°	110°	125°	140°	505 - 537	43 h	$.22 \times 10^6$
4.05	100°	115°	130°	145°	538 - 572	41 h	$.26 \times 10^6$
4.05	105°	120°	135°	150°	573 - 582	14 h	$.10 \times 10^6$
4.05	105°	120°	135°	150°	607 - 641	46 h	$.25 \times 10^6$
3.14	105°	120°	135°	150°	649 - 683 ³	31 h	$.34 \times 10^6$
3.14	105°	120°	135°	150°	687 - 707	25 h	$.34 \times 10^6$
3.14	100°	115°	130°	145°	708 - 719	13 h	$.13 \times 10^6$
3.14	100°	115°	130°	145°	741 - 765	31 h	$.23 \times 10^6$
3.14	100°	115°	130°	145°	788 - 792	6 h	$.04 \times 10^6$
3.14	100°	115°	130°	145°	794 - 836	59 h	$.97 \times 10^6$
3.14	95°	110°	125°	140°	840 - 874	60 h	1.17×10^6

Table 4.2: A list of the 617 runs for which data was acquired while using the DAQ2 workstation. Again, superscripts indicate missing runs (or data) as detailed in Table 4.3.

E_n^{lab}	θ_1^{lab}	θ_2^{lab}	θ_3^{lab}	θ_4^{lab}	Run nos.	Duration	Events
3.14	30°	50°	70°	90°	446 - 458 ⁴	21 h	$.70 \times 10^6$
3.14	30°	50°	70°	90°	461 - 474	24 h	1.52×10^6
3.14	25°	45°	70°	90°	475 - 478	11 h	1.05×10^6
3.14	25°	45°	65°	90°	479 - 485	12 h	1.34×10^6
3.14	20°	40°	65°	90°	486 - 489	7 h	1.04×10^6
3.14	20°	40°	65°	85°	490 - 503 ⁵	22 h	2.61×10^6
3.14	23°	43°	60°	85°	504 - 512	25 h	3.07×10^6
3.14	35°	55°	70°	85°	513 - 517	13 h	1.28×10^6
3.14	35°	55°	75°	90°	518 - 530 ⁶	33 h	3.00×10^6
3.14	35°	55°	75°	90°	536 - 542	15 h	1.97×10^6
3.14	27°	47°	63°	80°	543 - 553	27 h	3.22×10^6
2.26	30°	50°	70°	90°	555 - 564	24 h	2.03×10^6
3.14	27°	47°	63°	80°	566 - 573	23 h	1.03×10^6
2.26	30°	50°	70°	90°	656 - 671	32 h	$.85 \times 10^6$
2.26	27°	45°	65°	85°	673 - 698 ⁷	40 h	2.20×10^6
2.26	25°	40°	60°	80°	700 - 725	49 h	2.92×10^6
2.26	20°	35°	55°	75°	727 - 751	43 h	4.19×10^6
2.26	15°	35°	55°	75°	754 - 756	4 h	$.49 \times 10^6$
2.26	15°	30°	50°	—	757 - 760 ⁸	9 h	$.99 \times 10^6$
2.26	95°	110°	125°	140°	779 - 835 ⁹	126 h	1.90×10^6
2.26	100°	115°	130°	145°	854 - 917 ¹⁰	147 h	1.84×10^6
2.26	100°	115°	130°	145°	965 - 975	23 h	1.40×10^6
2.26	105°	120°	135°	150°	976 - 996	45 h	2.36×10^6
2.26	105°	120°	135°	150°	1000 - 1009	19 h	$.13 \times 10^6$
1.60	105°	120°	135°	150°	1012 - 1061	101 h	1.38×10^6
1.60	100°	115°	130°	145°	1062 - 1104	93 h	1.01×10^6
1.60	95°	110°	125°	140°	1105 - 1108	9 h	$.10 \times 10^6$
1.60	95°	110°	125°	140°	1126 - 1127	5 h	$.05 \times 10^6$
1.60	95°	110°	125°	140°	1128 - 1155	60 h	$.55 \times 10^6$
1.60	95°	110°	125°	140°	1156 - 1179	58 h	$.46 \times 10^6$
1.60	45°	60°	75°	90°	1181 - 1192	23 h	$.51 \times 10^6$
1.60	45°	60°	75°	90°	1193 - 1204	22 h	$.52 \times 10^6$
1.60	40°	55°	70°	85°	1205 - 1224	37 h	1.02×10^6
1.60	35°	50°	70°	85°	1225 - 1226	4 h	$.11 \times 10^6$
1.60	35°	50°	65°	80°	1227 - 1235	16 h	$.49 \times 10^6$
1.60	35°	50°	65°	80°	1236 - 1241	12 h	$.40 \times 10^6$
1.60	30°	50°	65°	80°	1242 - 1245	7 h	$.23 \times 10^6$
1.60	30°	47°	65°	80°	1246 - 1253	12 h	$.37 \times 10^6$
1.60	19°	30°	47°	60°	1313 - 1327	26 h	$.67 \times 10^6$
1.60	19°	30°	47°	65°	1328 - 1332	12 h	$.30 \times 10^6$

Table 4.3: An addendum to Tables 4.1 and 4.2, indexed by superscript.

Superscript	Note
1	Run 135 omitted
2	Runs 178, 184 omitted
3	Runs 664, 670 omitted
4	Run 447 omitted
5	Runs 499, 500 omitted
6	Run 525 omitted
7	Due to a malfunction with the PSD module for R2, runs 679 - 681, while included in this tabulation, were selectively excluded from contributing to the second detector pair
8	While the fourth detector pair was positioned at $\theta_{\text{lab}} = 70^\circ$, it was not possible to obtain a recoil spectrum with the chosen ^3He cell HV
9	Runs 795, 796 omitted
10	Runs 876, 885, 886 omitted

Table 4.4: Cumulative time for which detectors were operated at each angle for each incident neutron energy over the course of the experiment. Note that the total time spent at a given energy is (with the unremarkable exception of 2.26 MeV) one-fourth the sum of the times spent at the individual angles, due to four detector pairs nearly always being measured simultaneously.

θ_{lab}	Energy in MeV				
	5.54	4.05	3.14	2.26	1.60
15°	—	—	—	13 h	—
19°	—	—	—	—	37 h
20°	15 h	51 h	29 h	43 h	—
23°	—	—	25 h	—	—
25°	19 h	30 h	22 h	49 h	—
27°	—	—	50 h	40 h	—
28°	12 h	—	—	—	—
30°	30 h	78 h	45 h	65 h	57 h
35°	15 h	45 h	62 h	47 h	32 h
40°	19 h	36 h	29 h	49 h	37 h
43°	—	—	25 h	—	—
45°	12 h	45 h	22 h	40 h	45 h
47°	—	—	50 h	—	50 h
50°	30 h	78 h	45 h	65 h	39 h
55°	15 h	45 h	62 h	47 h	37 h
60°	19 h	36 h	25 h	49 h	71 h
63°	—	—	50 h	—	—
65°	12 h	45 h	40 h	40 h	59 h
70°	30 h	78 h	69 h	56 h	41 h
75°	15 h	45 h	49 h	47 h	45 h
80°	19 h	51 h	50 h	49 h	47 h
85°	12 h	55 h	60 h	40 h	41 h
90°	38 h	98 h	123 h	56 h	45 h
95°	26 h	57 h	60 h	126 h	132 h
100°	22 h	41 h	108 h	171 h	93 h
105°	22 h	60 h	56 h	64 h	101 h
110°	26 h	57 h	60 h	126 h	132 h
115°	22 h	41 h	108 h	171 h	93 h
120°	22 h	60 h	56 h	64 h	101 h
125°	26 h	57 h	60 h	126 h	132 h
130°	22 h	41 h	108 h	171 h	93 h
135°	22 h	60 h	56 h	64 h	101 h
140°	26 h	57 h	60 h	126 h	132 h
145°	22 h	41 h	108 h	171 h	93 h
150°	14 h	60 h	56 h	64 h	101 h
Tot.:	147 h	362 h	457 h	563 h	496 h

Data Reduction and Analysis

5.1 Overview

In order to obtain values for the analyzing power from the signals' characteristics that have been collected by the DAQ, various data reduction procedures are required. Of greatest importance in an analyzing power measurement is the exclusion of events corresponding to processes other than the elastic scattering of neutrons by helium. Due to the insensitivity to the efficiency (equally of detection or identification of neutrons) in any given detector, so long as that efficiency is consistent between spin "states" of the beam, the rejection of events of interest becomes a concern primarily of precision, not accuracy (as it would have been in a cross section measurement).

As data was obtained in the format of "events" consisting of readouts of all relevant channels upon the reception of a trigger, the data content of a run is essentially a distribution of points¹ in an n -dimensional space (with n the number of channels being recorded); data reduction for the most part proceeded by taking a projection

¹ Colloquially "ntuples;" in more exact terminology, the data content is an integer-valued distribution, to account for the rare case of two "events" with identical coordinates (for which a "point" is a computationally inaccurate description).

of this distribution onto a single variable (exceptions taking the form of a projection onto the plane of two variables), determining an interval of valid values for that variable (hereafter referred to as a “window”), and subsequently removing all “events” with values of that variable outside of that interval from further analysis.

Two analyses were conducted on the data, one using the PAW++ analysis package, another ROOT. In the former, all windows were set manually; in the latter, only in the case of the PSD parameter was this determination purely manual, with parameters from curve fits being used to calculate bounds at one twentieth the maximal height (as determined by the fit) of the peaks in the flight-time and recoil-energy spectra.

Despite different implementations, the order in which observables were analyzed and windows thereof determined in the course of data reduction for the primary array was consistently maintained: for events in coincidence with a particular side detector, a window was set first for the PSD parameter, followed by two windows for flight times, one for the neutrons of interest and another to provide an estimate of the accidental background; a window, this time made common to all coincidences with either of a particular detector pair, in the resulting ^3He recoil spectra concluded this stage (and method) of analysis, with the selected events being counted and the sums being entered into the formula for the analyzing power.² This was done individually for each CODA run; all values thus obtained for a particular energy and angle were added in quadrature to arrive at the results presented in the Summary.

² Albeit with some modification due to accidental subtraction.

5.2 Description of Methods

5.2.1 Primary Array

Pulse-shape Discrimination

To determine the window on the PSD parameter, an examination was first made of the projection of the unfiltered entirety of events for a run onto the Cartesian product of the PSD parameter and center-side flight time for a given side detector; one such projection is displayed in Fig. 5.1. Neutrons and photons are generally present as two distinct peaks,³ the former with higher values of both mean PSD parameter and mean flight time. As an arbitrarily high PSD parameter is most likely to correspond to a neutron, the interval chosen for the PSD window was without upper bound; the lower bound was generally chosen to exclude as many photons as possible from further analysis, but not at the expense of a significant fraction of the neutron total.

Flight-Time Selection

As was first implemented in the ROOT-based analysis, the determination of the flight-time window was largely not done manually, but instead relied on a curve fit; for the flight-time peaks observed, it was determined that, with the addition of a flat background, a Gaussian function would provide an adequate fit function (with fit parameters being the amplitude of the background, and the amplitude, “mean,” and “standard deviation”⁴ of the Gaussian). A spectrum first being obtained by projection onto the flight-time axis of a given side detector (in accordance with the relevant PSD window), a fiducial value was chosen by eye and an interval of 200

³ A complication arising from an unsupervised strobe setting resulted in some photon peaks being wholly absorbed in an accumulation corresponding to the minimum output of the PSD module; in further cases, thresholds on the side detectors were sufficiently high to obscure any such peak. Due to the always adequate resolution of the TDC, regardless of the PSD parameter distribution, the peaks are clearly distinguishable whenever present.

⁴ Despite some excellent analogies to the probability distribution, these two quantities referred to later are best defined respectively as μ and σ , where the form of the fit function was $B + A \exp\left(-\frac{(t-\mu)^2}{2\sigma^2}\right)$, t being the flight-time.

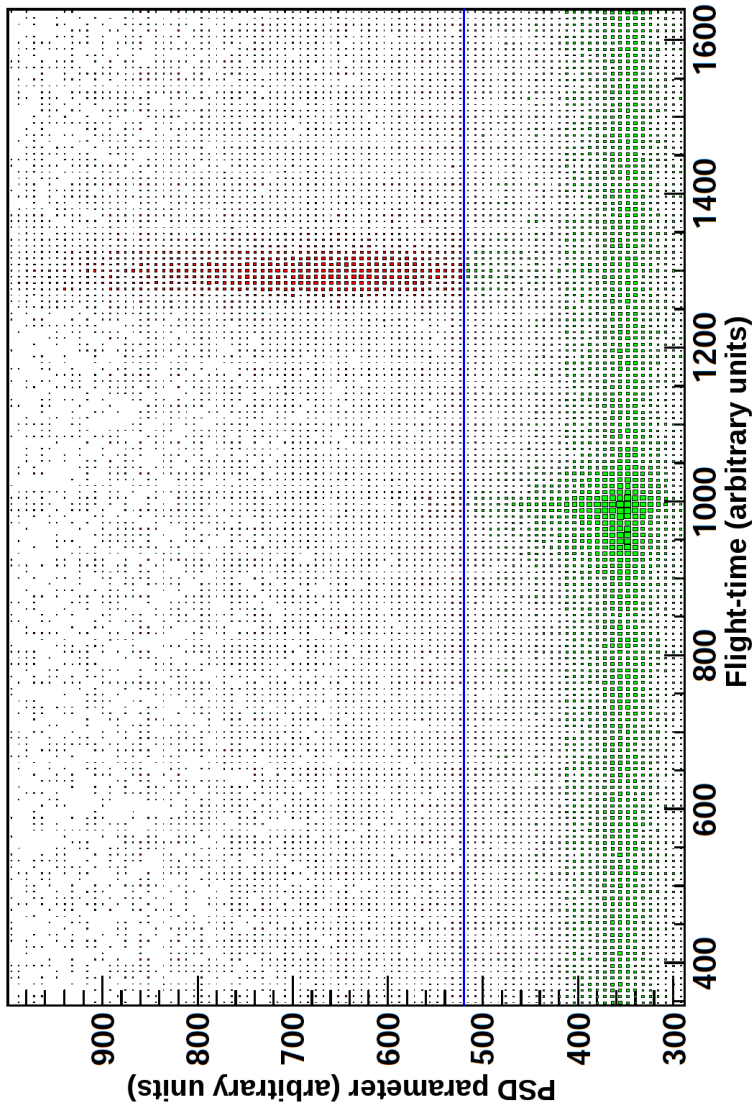


FIGURE 5.1: A histogram of the joint distribution of pulse-shape discrimination parameter p versus flight time (for R4 over runs 673 - 698 on DAQ2). The blue line at $p = 520$ represents the window used in analysis, with all points (highlighted in red) with p exceeding 520 being retained for further analysis, and all other points (highlighted in green) being eliminated therefrom. Note the green coloration (and hence exclusion) of the peak with both shorter flight time and smaller p , consequently identifiable as photons; the peak in red (signifying retention) has both higher p and longer flight-time, identifying it as neutrons. Not shown due to an anomalous distribution in p are a large number of counts with p short of 288, which are eliminated by the PSD window.

channels surrounding it (but excluding any pile-up that would interfere, as would otherwise have been occasional) was used as the domain for the fit. The bounds of the window used to select the neutrons of interest were taken to be the abscissae corresponding to values of the Gaussian one twentieth its maximum amplitude⁵.

Due to the expected uniformity of the distribution of accidentals in the flight-time spectrum, as well as the isolation from extraneous reactions afforded by the unphysical ranges thereof (as any events with a flight-time shorter than photons would imply a problematically supraluminal speed), a presumedly representative sample of accidental ^3He recoil energies was obtained for each detector through the application of a manually determined flight-time window. To take advantage of the aforementioned “signal” isolation, the bounds of the window were assigned to flight times preceding the photon peak whenever possible; in the instances when this was not possible (primarily due to insufficient delay in the side-detector-generated “stop” signal), the bounds were chosen for flight times sufficiently large that the distribution was approximately constant (and presumably overwhelmingly due to accidental background).

^3He Recoil Energy Selection

For the coincidences associated with each side detector, two ^3He recoil spectra were obtained by projection with the application of the newly-determined flight-time window, the previously established PSD window, and a spin condition. The spin state, as generated by the TUNL Communicator, was stored in effective a four-channel output, with either spin state being recorded distinctly and separately between the primary and polarimeter arrays. That for each spin state a distinct spectrum was generated was motivated by desire to have a graphical representation of the distributions that directly yield $N_{S\uparrow}$ under (partial) summation.

⁵ $\mu \pm \sqrt{2 \ln 20} \sigma$ in the previous footnote’s notation; for reference, $\sqrt{2 \ln 20} \approx 2.45$.

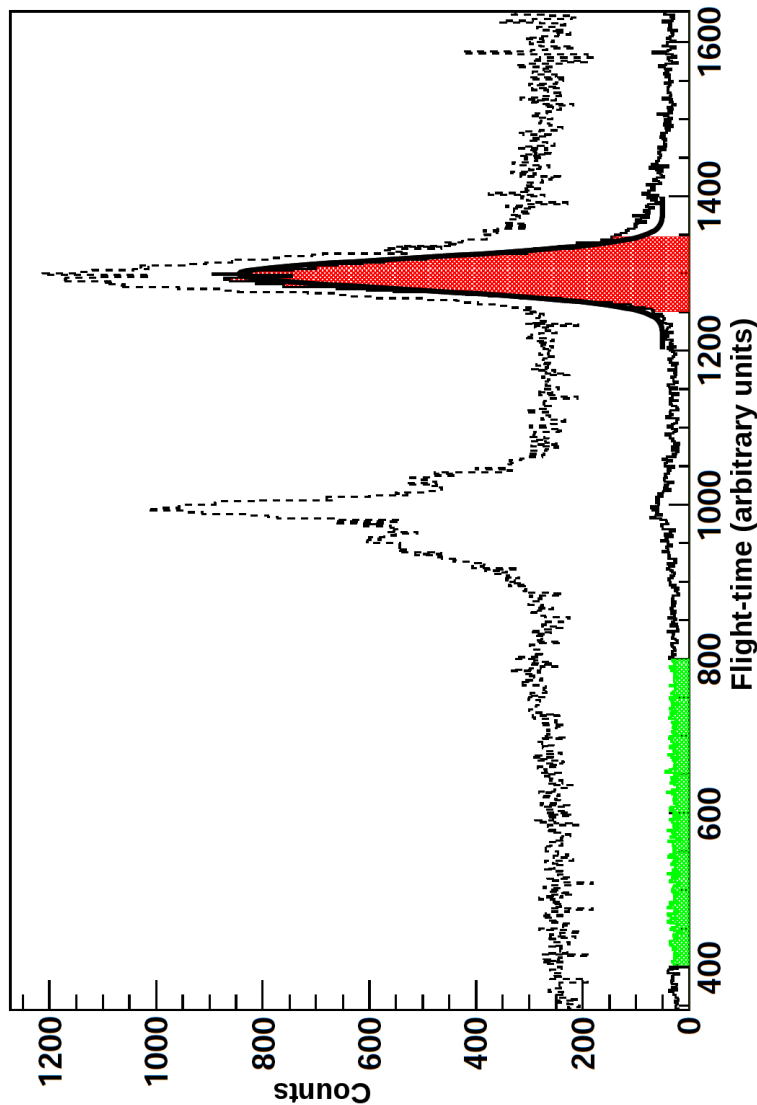


FIGURE 5.2: The flight-time spectrum of coincidences between the ^3He cell and R4 for runs 673 - 698 on DAQ2. The projection of the unfiltered (“raw”) distribution is displayed in dashes; the effect of an applied PSD “window” is displayed with a solid line. Note the resulting exclusion of nearly all of the gamma peak centered around channel 1000 in the raw spectrum. The Gaussian fit (with an assumed constant background) to the reduced distribution is displayed in bold. The flight-time windows for accidentals and valid counts are highlighted in green and red, respectively (shaded areas to the left and right for grayscale).

The determination of bounds for the window (which, at this stage of analysis, served as bounds of summation) in the ^3He recoil spectra took into account the expectation that, at equal howsoever opposite scattering angles, the recoil energies are identical: to maximize statistics for a curve fit, all four spectra corresponding to a given angle pair were summed, a fiducial value for the mean assigned by eye, and the spectrum fit with the function $f(E)$, E being the recoil energy, as given in Eq. 5.1:

$$f(E) = A \exp \left(-\frac{(E - \mu)^2}{2\sigma^2} + B \frac{E - \mu}{C + (E - \mu)^2} \right). \quad (5.1)$$

The bounds for the window were then found by solving for E such that f was maximized (with a corresponding exponent λ), and thereafter for E for which the exponent in Eq. 5.1 equalled $\lambda - \ln 20$ (while more than the desired two solutions were theoretically possible, such a situation was never encountered during analysis, owing to the relative smallness of B in the fits). This maintained the goal of setting gates at one twentieth the maximal heights of each of the flight-time and ^3He recoil peaks.

Such a skewed Gaussian was chosen due to the strongly asymmetrical peak structure in some ^3He recoil spectra; this in turn was due to cross section⁶ that varied rapidly with angle.

5.2.2 Polarimeter

Due to a smaller dynamic range of the TAC's and the frequent (and negligent) gain mismatches of the ^4He cell PMT's, it was decided not to automate the window determination process for the polarimeter, but to perpetuate manual determination as used in the PAW++ analysis.

⁶ With a contribution from analyzing power, despite the relatively small polarization.

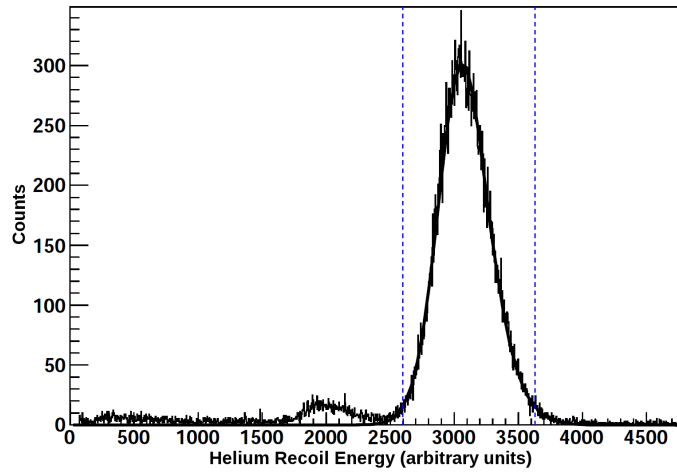


FIGURE 5.3: The sum of the ${}^3\text{He}$ recoil spectra separately obtained in coincidence with either of the R4 and L4 neutron detectors, without spin-state selection, but with PSD and flight-time selection having been applied. The data set is once again runs 673 - 698 taken with DAQ2. A fit using the function f from Eq. 5.1 and the resulting bounds at one twentieth maximal height are displayed in bold and dashed blue, respectively.

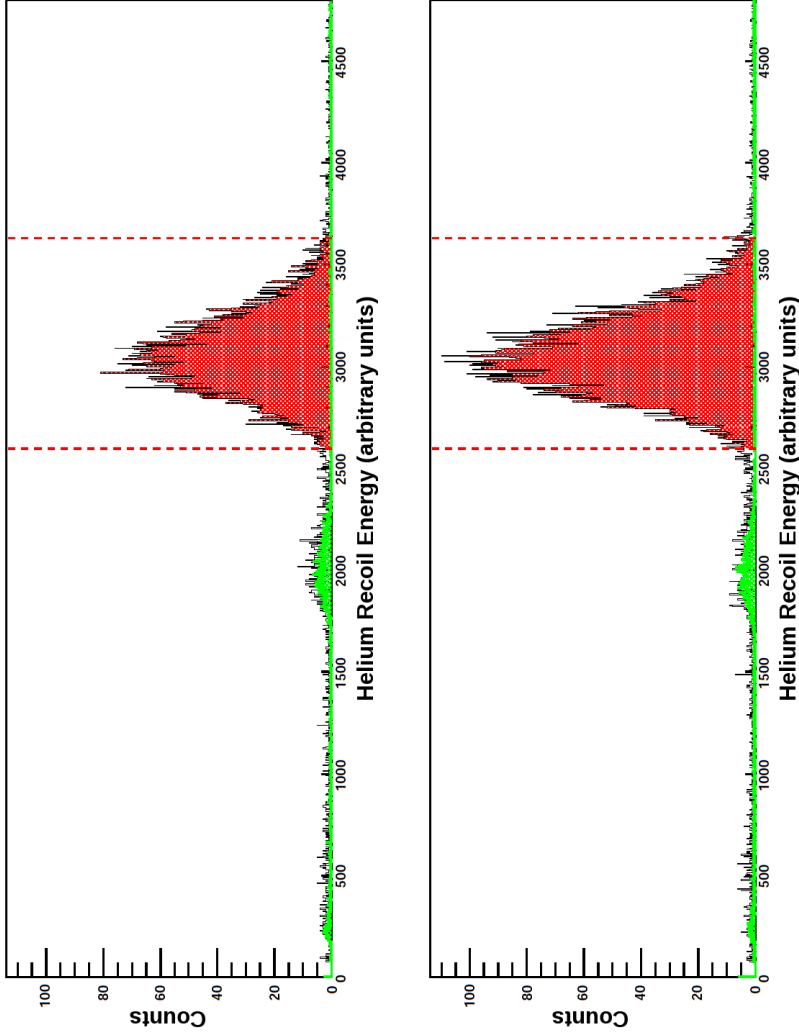


FIGURE 5.4: ^3He recoil spectra obtained in coincidence with R4 for runs 673 - 698 on DAQ2; the upper spectra have spin state up selected, as the lower have spin state down. For each plot, the spectrum corresponding to the “valid” neutron flight-time region is outlined in black, with the region within the recoil energy window determined in Fig. 5.3 highlighted in red (with the gates themselves delineated in dashed red). The spectrum in each plot obtained from the designated flight-time region for accidentals is displayed in green. A normalization factor has been applied to account for the discrepancy in time intervals between the two flight-time windows: the “valid” and accidental spectra as presented are additively comparable. Note the peak centered around 764 keV resulting from the $^3\text{He}(n,pt)$ reaction; accidental subtraction for the peak yielded a value slightly but significantly higher than the expected value of zero.

Monte Carlo Simulations

6.1 Monte Carlo Simulations and Corrections

An accurate comparison between data obtained with our particular arrangement of target and detectors, each with spatial extent, and theoretical calculations at precise scattering angles for a specific interaction requires compensation for this difference in configuration and physical scope. This was achieved by examining the effects on fiducial values of the analyzing power in a Monte Carlo simulation, undertaken by [Tor12] and included here as background material, which took into account the array geometry and a broader range of reactions capable of contributing to the measured neutron signal. A forced-collision routine was used, following the method outlined in [Tor75], in which particle trajectories were constrained to intersect the detector; the neutron fluence due to various processes was obtained through successive evaluations of differential cross sections (and the density matrix of the scattered neutrons) at collision points.

As a presumed improvement over the predictions of existing theoretical or empirical models of the analyzing power, curve fits to the results of data analysis were

used as a fiducial value for the n - ^3He analyzing power in the Monte Carlo simulation; all cross sections were obtained from literature values. Distributions in flight-time and ^3He recoil energy corresponding to the neutron fluence into a side detector due to single scattering were then obtained for a simulated perfectly polarized incident beam and observing the primary array geometry (with the exception of detector angles not multiples of five degrees in the lab). These distributions were then subjected to the same windows as applied in data reduction, resulting in asymmetries (here equivalent to analyzing powers) that deviated significantly but consistently by less than 10% of the analyzing power maximum from the fiducial values; to present such results clearly, the analyzing power differences from the fiducial values due to this treatment of “finite geometry” alone are shown in red for the five energies in Figs. 6.1, 6.2, 6.3, 6.4, and 6.5.

The double-scattering processes capable of contributing to the neutron signal were organized according to scattering media using a numbering scheme in which helium, xenon, iron in the gas cell wall, and iron in the gas cell flanges were assigned respectively the first four natural numbers, resulting in a two-digit label with the order of digits reproducing that of the corresponding scatterings; this is shown in Table 6.1. It is noted that, for double scattering, this list is exhaustive: due to the high atomic mass of xenon, and absence of significant contaminants in the scintillation volume, recoil from any reaction not involving ^3He , including single n - ^3Xe scattering, was too low in energy to be included in the final neutron enumeration. Furthermore, as the flange was not directly exposed to the neutron beam, it is only included as a second scattering medium. The same types of distributions were obtained as for single scattering, and windows applied accordingly, resulting in analyzing power differences shown in blue in Figs. 6.1, 6.2, 6.3, 6.4, and 6.5. It is noted that the differences due to double scattering are yet smaller than those due to finite geometry alone; of the various double scattering processes, it is noted that those involving iron contributed

Table 6.1: A summary of interaction designations for double scattering in the Monte Carlo simulation.

Designation	Interactions
11	$n\text{-}^3\text{He} \rightarrow n\text{-}^3\text{He}$
12	$n\text{-}^3\text{He} \rightarrow n\text{-Xe}$
21	$n\text{-Xe} \rightarrow n\text{-}^3\text{He}$
13	$n\text{-}^3\text{He} \rightarrow n\text{-Fe}_{\text{Wall}}$
31	$n\text{-Fe}_{\text{Wall}} \rightarrow n\text{-}^3\text{He}$
14	$n\text{-}^3\text{He} \rightarrow n\text{-Fe}_{\text{Flange}}$

most to the calculated fluence, due to the mass of the cell wall and flange being vastly greater than that of the gas.

While additive differences have been presented for ease of comparison, the compensation made to the results of analysis took the form of a multiplicative factor, $A_y^{\text{fid.}}/A_y^{\text{MC}}$, where $A_y^{\text{fid.}}$ is the fiducial analyzing power and A_y^{MC} is the result of the simulations. At angles not directly addressed by simulations, a linear interpolation of the correction factor was used.

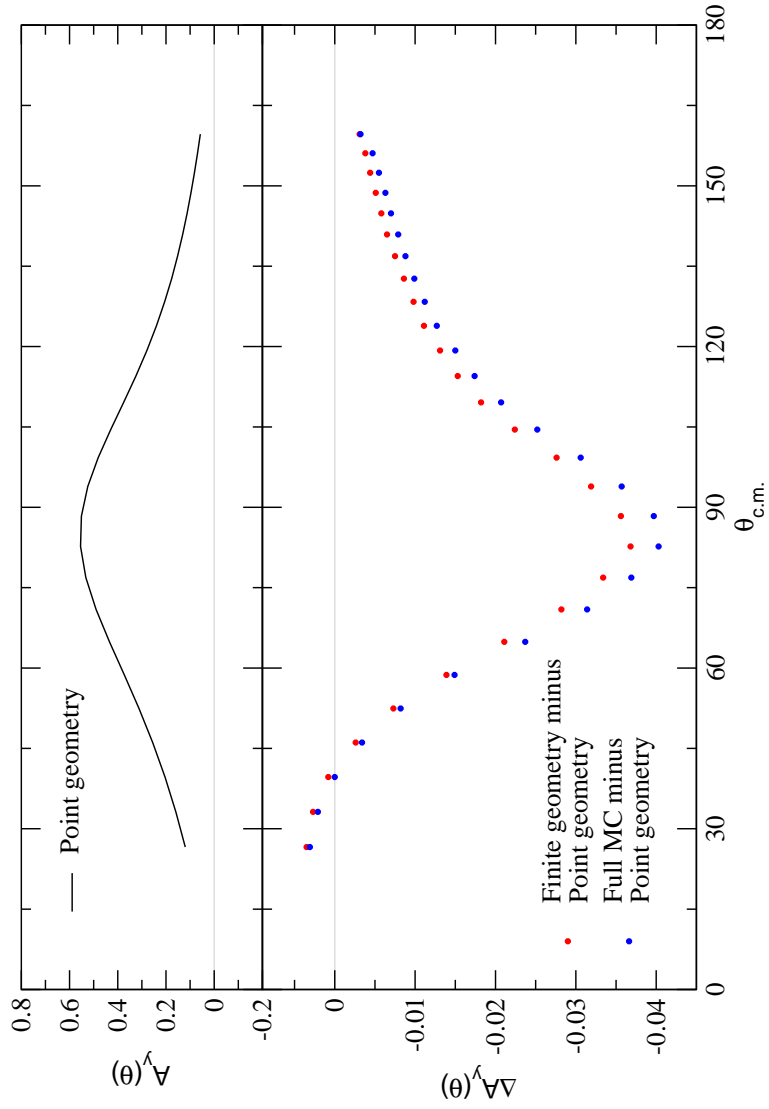


FIGURE 6.1: Above, the fiducial (“point geometry”) analyzing power and, below, the differences between it and results of Monte Carlo simulation for $E_n = 1.60$ MeV including (“full MC”) and excluding (“finite geometry”) multiple scattering contributions. It is noted that differences are roughly an order of magnitude less than values, as prompted this mode of presentation. The magnitude of the differences for this energy in particular is due to a shorter target-detector distance and a corresponding exacerbation of finite-geometry effects.

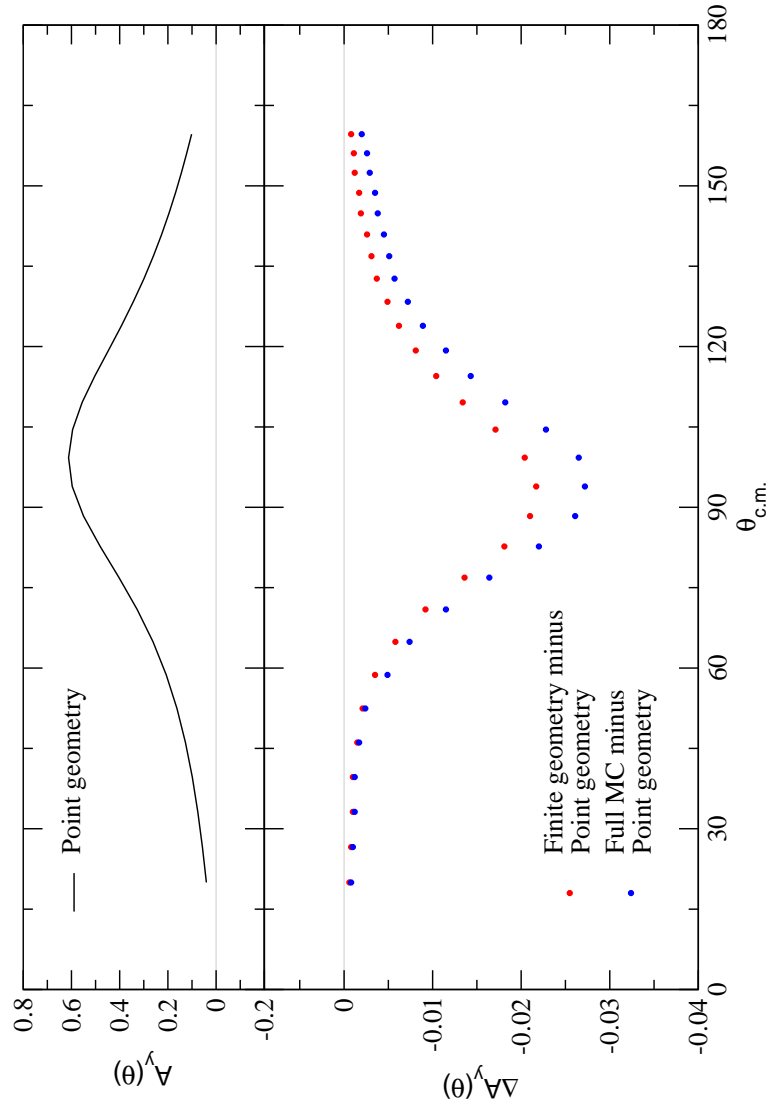


FIGURE 6.2: Fiducial analyzing power and differences as in Fig. 6.1, for $E_n = 2.26$ MeV.

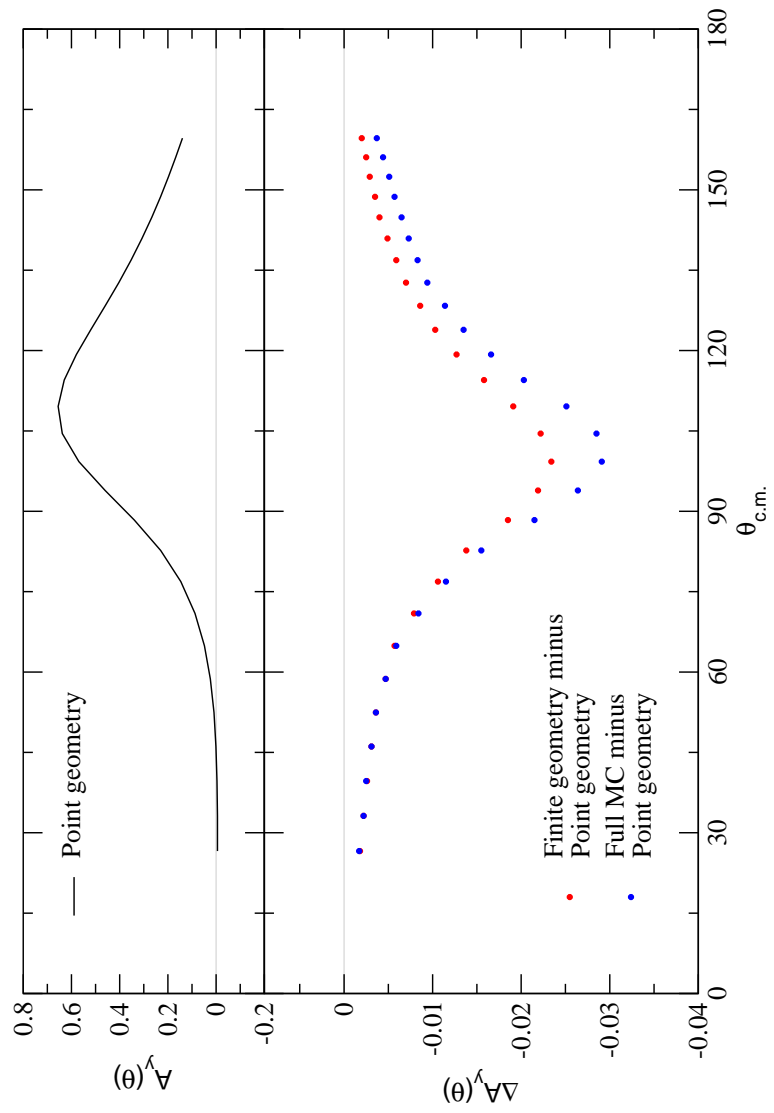


FIGURE 6.3: Fiducial analyzing power and differences as in Fig. 6.1, for $E_n = 3.14$ MeV.

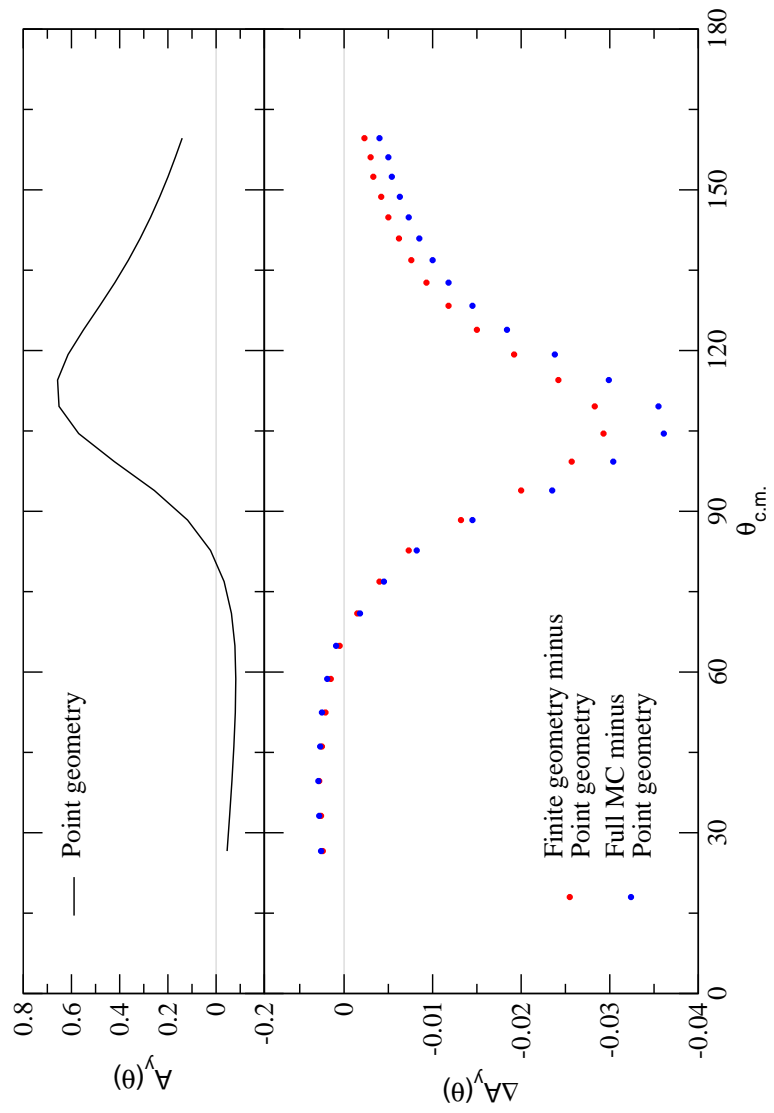


FIGURE 6.4: Fiducial analyzing power and differences as in Fig. 6.1, for $E_n = 4.05$ MeV.

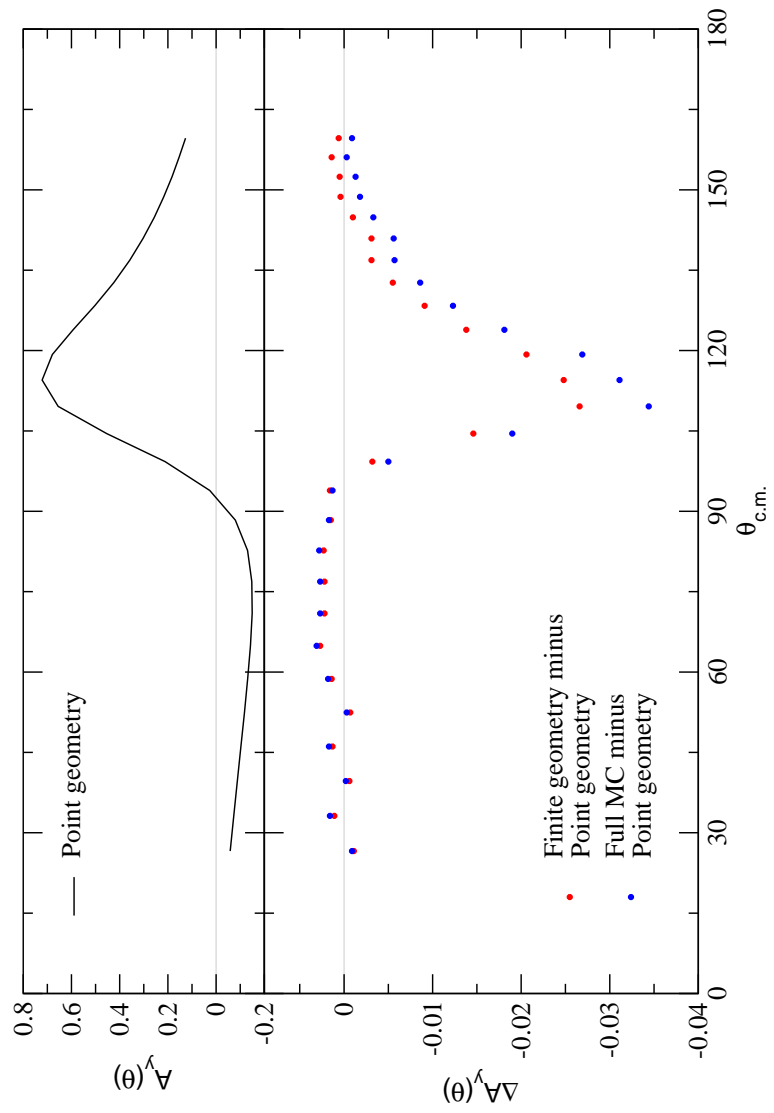


FIGURE 6.5: Fiducial analyzing power and differences as in Fig. 6.1, for $E_n = 5.54$ MeV.

Results and Summary

7.1 Presentation of Data

The results of data analysis, here the “raw” data (i.e., without corrections for finite geometry or multiple scattering and thus not directly comparable to theory), are presented in Table 7.1; with the application of multiplicative corrections as determined in the previous section, the inferred point geometry results of the present measurement are presented in Table 7.2. Uncertainties throughout this section represent statistical contributions only; systematic uncertainties were primarily due to uncertainties in the corrections determined by Monte Carlo simulations and those in the n - ^4He analyzing power used in the polarimetry. Of these two mentioned effects, the former is estimated to contribute an absolute value of .01 to the systematic uncertainty; the latter, a relative value of 1%. It is notable that (primarily accidental) background subtraction in data reduction was found to contribute minimally: even where the ^3He recoil distributions attributable to elastic neutron scattering and the $^3\text{He}(n, p)^3\text{H}$ reaction coincided, an artificial doubling of the accidental background

resulted in a .5% increase in the analyzing power.¹

The data, again omitting contributions to their uncertainties from these systematic effects, are presented in comparison with theoretical calculations in Figs. 7.1, 7.2, 7.3, 7.4, and 7.5.

7.2 Discussion of Results

The results of this measurement are found to be in disagreement with theoretical calculations particularly at analyzing power maxima at all incident neutron energies. It is however noted that away from the analyzing power maximum, differences, as directly presented in Fig. 7.6, at the lowest energy, $E_n = 1.60$ MeV, are largely not statistically significant between experimental values and calculations with only N - N interactions; however, the inclusion of the Δ -mediated 3NF brings calculations into more marked disagreement with the experimental values, particularly at backward angles. This is contrary to expectations that the inclusion of 3NF's would improve the accuracy of theoretical models. Calculations obtained using only the CD-Bonn potential model are generally in near agreement with the present data at forward angles for the lowest three energies, $E_n = 1.60, 2.26,$ and 3.14 MeV, as further evinced in Figs. 7.7 and 7.8, in contrast with calculations using the Argonne potential, which consistently underpredict the present data (at all angles, though more markedly at forward ones) and those incorporating the 3NF, which overpredict in this angular region. All three sets of calculations consistently, and increasingly with higher energy, underpredict measurement at angles in the vicinity of and higher than that corresponding to the analyzing power maximum.

The relation between calculations and measurement for the two highest energies, $E_n = 4.05$ and 5.54 MeV, is roughly proportional (this also applies to the lowest two energies, but with a constant of proportionality much closer to unity) with experimental results exceeding theoretical calculations by a factor of approximately

¹ From a limited sample of such distributions when well-separated, which enabled an accurate comparison of accidentals corresponding to the region of interest in flight-time to those corresponding to the purported accidental-only region in flight-time, a factor of 1.3 (1.34 ± 0.10) was the largest observed discrepancy, far short of the factor of two used here.

Table 7.1: Uncorrected (“raw”) results from data analysis for the n - ^3He analyzing power at all energies and angles entailed by the present work; where available, the center-of-mass angles for 3.14 MeV are used as approximations for those at other energies. ΔA_y denotes the statistical uncertainty in the given values.

$E_n^{\text{lab.}}$; \rightarrow	1.60 MeV		2.26 MeV		3.14 MeV		4.05 MeV		5.54 MeV	
	A_y^{raw}	ΔA_y^{raw}	A_y^{raw}	ΔA_y^{raw}	A_y^{raw}	ΔA_y^{raw}	A_y^{raw}	ΔA_y^{raw}	A_y^{raw}	ΔA_y^{raw}
$\theta_{c.m.} (^{\circ})$; \downarrow	19.974		0.0578	0.0143						
25.259	0.0858	0.0143	0.0563	0.0079	0.0139	0.0058	-0.0410	0.0061	-0.0594	0.0058
26.584					-0.012	0.0080				
30.527			0.0699	0.0081	-0.0060	0.0090	-0.0501	0.0104	-0.0800	0.0045
33.145			0.0859	0.0089	-0.0137	0.0063				
37.071									-0.0805	0.0046
39.649	0.2199	0.0154	0.0801	0.0078	-0.0024	0.0079	-0.0681	0.0061	-0.0837	0.0047
46.085	0.2502	0.0155	0.1222	0.0090	-0.0202	0.0094	-0.0786	0.0084	-0.1035	0.0057
52.442	0.3257	0.0144	0.1729	0.0100	0.0111	0.0095	-0.0822	0.0094	-0.1245	0.0052
56.214					0.0230	0.0100				
58.710	0.3674	0.0140	0.2365	0.0130	0.0404	0.0113	-0.0928	0.0101	-0.1261	0.0062
61.196	0.4072	0.0186			0.0185	0.0086				
64.877	0.4291	0.0149	0.2786	0.0129	0.0434	0.0113	-0.0765	0.0088	-0.1417	0.0070
70.934	0.5281	0.0169	0.3442	0.0158	0.1075	0.0138	-0.0679	0.0126	-0.1481	0.0096
76.871	0.5101	0.0154	0.4263	0.0183	0.1302	0.0150	-0.0091	0.0150	-0.1489	0.0089
79.195					0.1899	0.0131				
82.680	0.5727	0.0162	0.4867	0.0235	0.2303	0.0143	0.0614	0.0170	-0.1302	0.0113
88.352	0.5629	0.0184	0.5659	0.0230	0.3541	0.0169	0.1129	0.0155	-0.0584	0.0134
93.883	0.5137	0.0185	0.6409	0.0257	0.4115	0.0246	0.2403	0.0223	0.0395	0.0172
99.265	0.4587	0.0176	0.6586	0.0261	0.5884	0.0192	0.4266	0.0207	0.2196	0.0180
104.496	0.4352	0.0183	0.6224	0.0290	0.6556	0.0179	0.5270	0.0232	0.4099	0.0204
109.572	0.3678	0.0179	0.5700	0.0247	0.6200	0.0142	0.6232	0.0200	0.6215	0.0174
114.494	0.3324	0.0142	0.5331	0.0252	0.5869	0.0203	0.6463	0.0198	0.7028	0.0151
119.261	0.2641	0.0162	0.4455	0.0283	0.5696	0.0202	0.6333	0.0211	0.6640	0.0144
123.877	0.2373	0.0148	0.4177	0.0146	0.4719	0.0196	0.5570	0.0213	0.5968	0.0126
128.345	0.1930	0.0189	0.3471	0.0230	0.4736	0.0175	0.4849	0.0180	0.4978	0.0127
132.670	0.1643	0.0168	0.3247	0.0271	0.4083	0.0182	0.4562	0.0192	0.4298	0.0120
136.860	0.2030	0.0154	0.3067	0.0156	0.3400	0.0184	0.3550	0.0200	0.3735	0.0106
140.922	0.1189	0.0184	0.2406	0.0230	0.2890	0.0177	0.3139	0.0171	0.3037	0.0110
144.865	0.1338	0.0154	0.2003	0.0204	0.2493	0.0182	0.2762	0.0186	0.2611	0.0107
148.698	0.0905	0.0137	0.1880	0.0155	0.1943	0.0184	0.2183	0.0201	0.2136	0.0098
152.430	0.0649	0.0143	0.1448	0.0211	0.2009	0.0160	0.1954	0.0155	0.1907	0.0097
156.074	0.0632	0.0168	0.1000	0.0209	0.1678	0.0167	0.1543	0.0173	0.1571	0.0098
159.639	0.0617	0.0149	0.1128	0.0195	0.1359	0.0167	0.1349	0.0185	0.1373	0.0111

Table 7.2: Inferred point geometry results of the present experiment, obtained by applying multiplicative corrections determined from Monte Carlo simulations, presented as in Table 7.1.

$E_{n.}^{\text{lab.}} \rightarrow$ $\bar{\theta}_{\text{c.m.}} (^{\circ}) \downarrow$	1.60 MeV		2.26 MeV		3.14 MeV		4.05 MeV		5.54 MeV	
	A_y	$\Delta A_y^{\text{cor.}}$	$A_y^{\text{cor.}}$	$\Delta A_y^{\text{cor.}}$	$A_y^{\text{cor.}}$	$\Delta A_y^{\text{cor.}}$	$A_y^{\text{cor.}}$	$\Delta A_y^{\text{cor.}}$	$A_y^{\text{cor.}}$	$\Delta A_y^{\text{cor.}}$
19.974			0.0590	0.0146						
25.259	0.0837	0.0139								
26.584			0.0573	0.0080	0.0106	0.0044	-0.0435	0.0065	-0.0585	0.0057
30.527					-0.0088	0.0059				
33.145			0.0710	0.0082	-0.0043	0.0064	-0.0527	0.0106	-0.0818	0.0045
35.755			0.0871	0.0090	-0.0091	0.0042				
37.071									-0.0811	0.0046
39.649	0.2199	0.0154	0.0811	0.0079	-0.0014	0.0047	-0.0712	0.0064	-0.0836	0.0047
46.085	0.2537	0.0157	0.1239	0.0091	0.0048	0.0023	-0.0816	0.0087	-0.1053	0.0058
52.442	0.3345	0.0148	0.1755	0.0102	0.0185	0.0158	-0.0848	0.0097	-0.1241	0.0052
56.214					0.0325	0.0141				
58.710	0.3828	0.0146	0.2422	0.0133	0.0503	0.0141	-0.0951	0.0103	-0.1279	0.0063
61.196	0.4269	0.0195			0.0222	0.0103				
64.877	0.4540	0.0158	0.2867	0.0133	0.0494	0.0129	-0.0775	0.0089	-0.1448	0.0071
70.934	0.5640	0.0180	0.3566	0.0164	0.1189	0.0153	-0.0661	0.0123	-0.1508	0.0098
76.871	0.5478	0.0165	0.4442	0.0191	0.1413	0.0163	-0.0080	0.0132	-0.1517	0.0090
79.195					0.2046	0.0141				
82.680	0.6174	0.0175	0.5101	0.0246	0.2469	0.0153	0.0950	0.0263	-0.1331	0.0115
88.352	0.6068	0.0198	0.5942	0.0241	0.3782	0.0180	0.1287	0.0176	-0.0597	0.0137
93.883	0.5512	0.0199	0.6717	0.0269	0.4366	0.0261	0.2646	0.0246	0.0377	0.0164
99.265	0.4899	0.0188	0.6882	0.0273	0.6202	0.0202	0.4599	0.0223	0.2248	0.0185
104.496	0.4622	0.0194	0.6473	0.0302	0.6864	0.0187	0.5628	0.0248	0.4279	0.0213
109.572	0.3891	0.0189	0.5894	0.0255	0.6448	0.0148	0.6593	0.0212	0.6557	0.0184
114.494	0.3513	0.0150	0.5486	0.0259	0.6063	0.0210	0.6773	0.0208	0.7344	0.0157
119.261	0.2792	0.0171	0.4571	0.0290	0.5861	0.0208	0.6586	0.0220	0.6912	0.0150
123.877	0.2506	0.0156	0.4273	0.0149	0.4846	0.0201	0.5765	0.0220	0.6153	0.0130
128.345	0.2042	0.0200	0.3544	0.0235	0.4854	0.0179	0.4999	0.0185	0.5103	0.0130
132.670	0.1740	0.0178	0.3309	0.0276	0.4181	0.0186	0.4695	0.0197	0.4389	0.0122
136.860	0.2154	0.0163	0.3128	0.0159	0.3482	0.0188	0.3649	0.0205	0.3795	0.0108
140.922	0.1265	0.0196	0.2454	0.0235	0.2959	0.0181	0.3227	0.0176	0.3094	0.0112
144.865	0.1426	0.0164	0.2043	0.0208	0.2555	0.0187	0.2839	0.0191	0.2645	0.0109
148.698	0.0968	0.0147	0.1919	0.0158	0.1992	0.0189	0.2244	0.0206	0.2155	0.0099
152.430	0.0696	0.0153	0.1478	0.0215	0.2063	0.0164	0.2009	0.0159	0.1920	0.0098
156.074	0.0678	0.0180	0.1022	0.0214	0.1723	0.0172	0.1589	0.0178	0.1574	0.0098
159.639	0.0653	0.0158	0.1151	0.0199	0.1396	0.0172	0.1388	0.0191	0.1383	0.0112

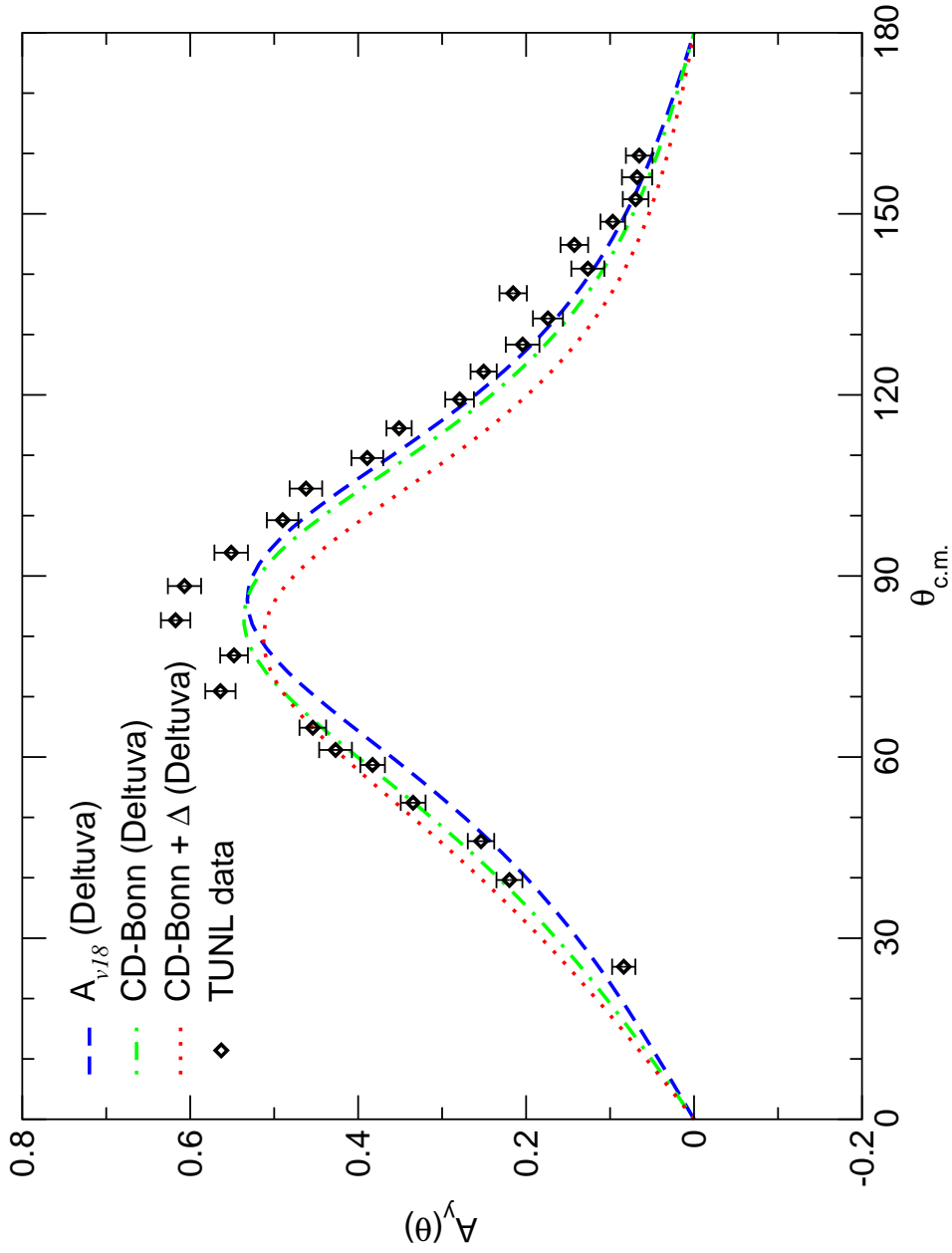


FIGURE 7.1: The n - ^3He analyzing power at $E_n = 1.60$ MeV measured in the present work (“TUNL data”), including multiplicative corrections determined from Monte Carlo simulations, along with theoretical calculations using the Argonne v_{18} and CD-Bonn N - N potential models, as well as the latter supplemented by a Δ -mediated $3N$ potential.

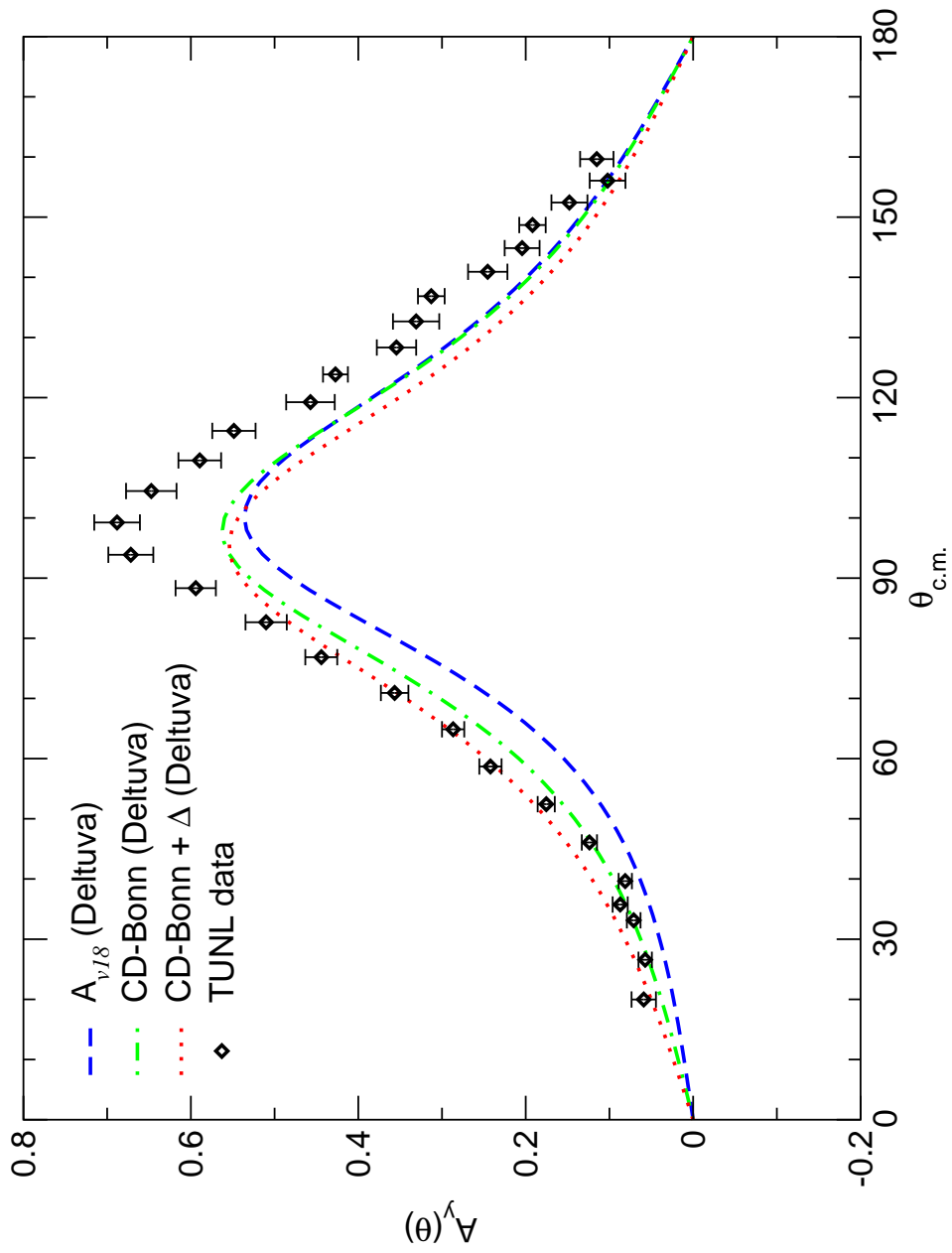


FIGURE 7.2: Measurement and theoretical calculation for the n - ^3He analyzing power at $E_n = 2.26$ MeV as presented in Fig. 7.1.

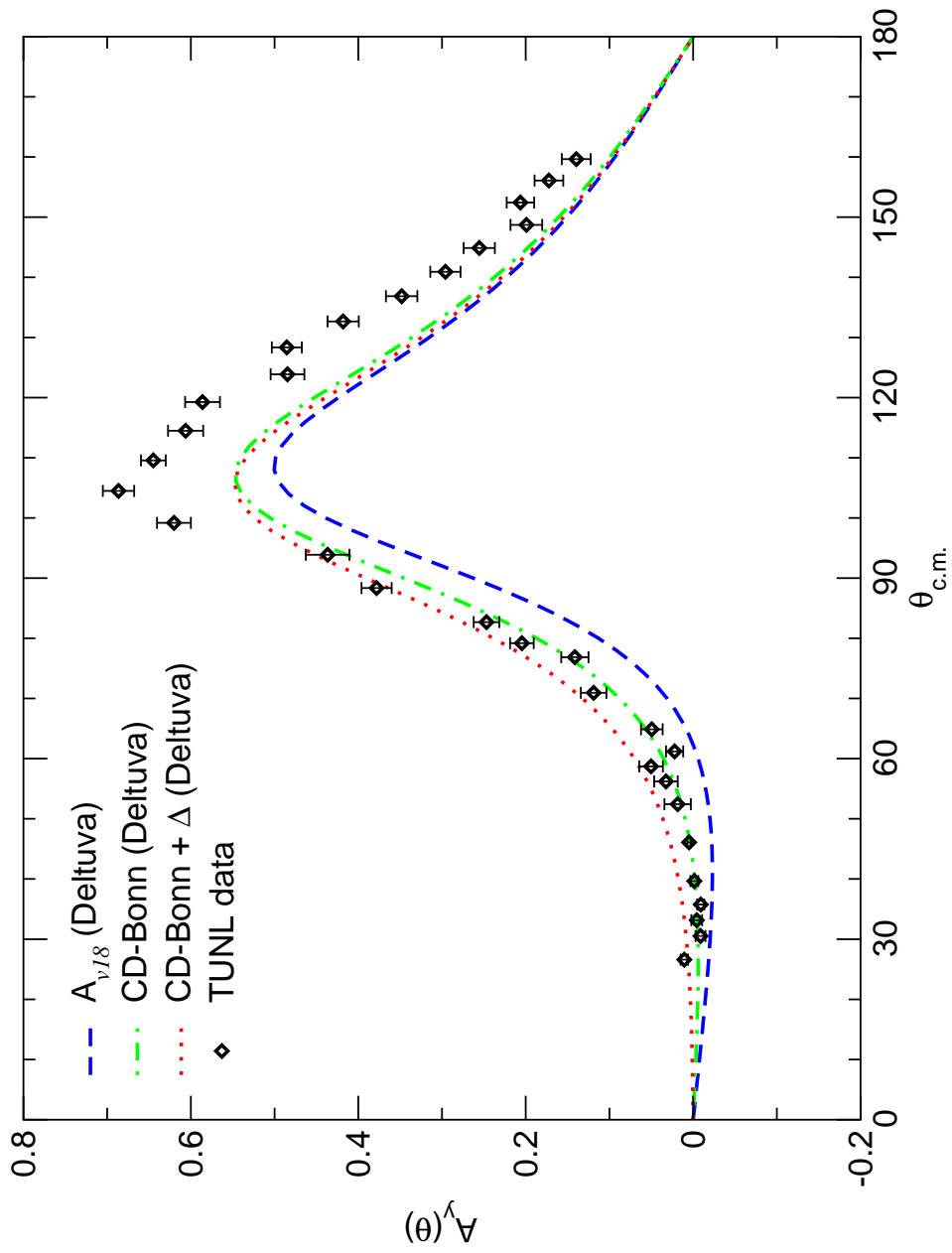


FIGURE 7.3: Measurement and theoretical calculation for the n - ^3He analyzing power at $E_n = 3.14$ MeV as presented in Fig. 7.1.

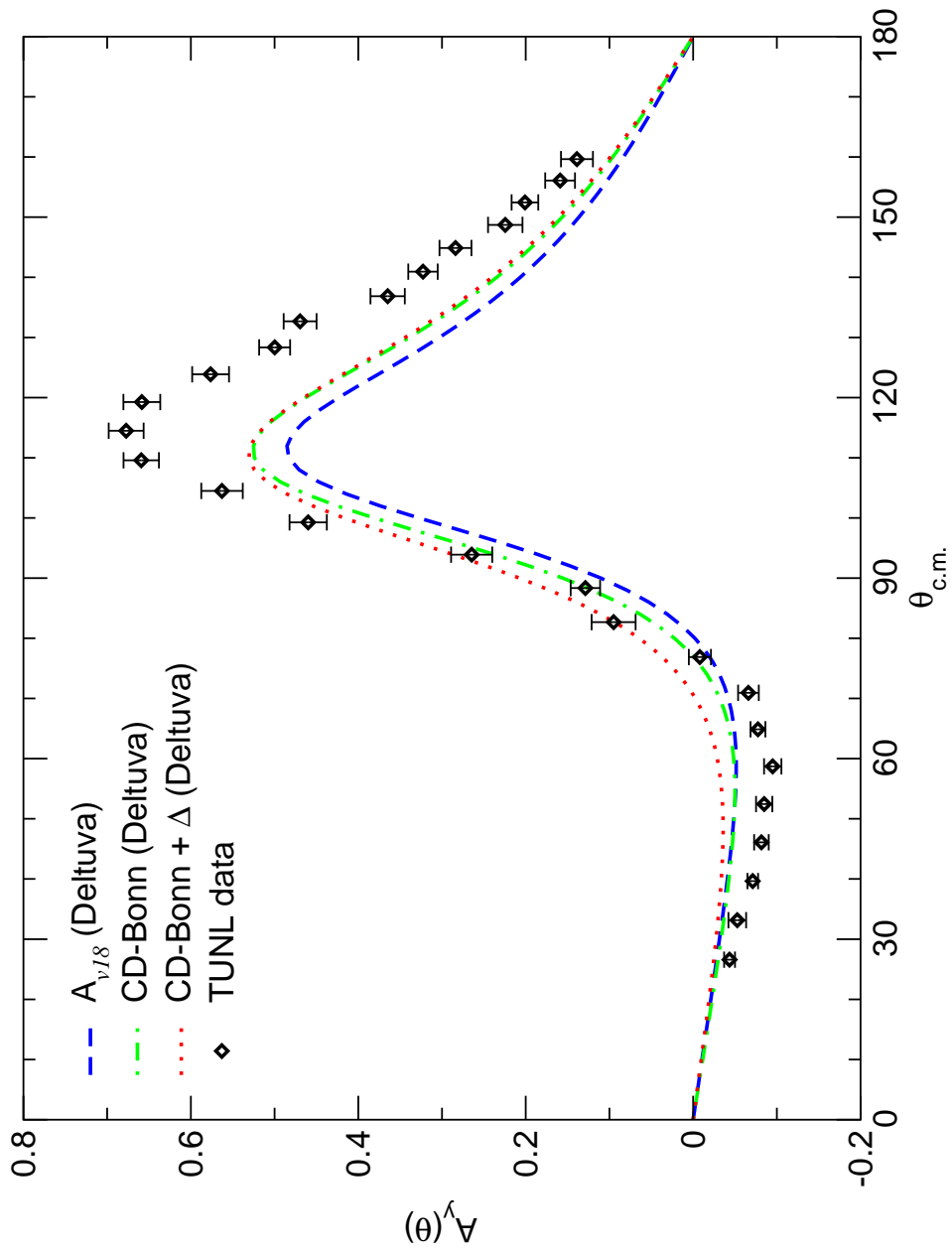


FIGURE 7.4: Measurement and theoretical calculation for the n - ^3He analyzing power at $E_n = 4.05$ MeV as presented in Fig. 7.1.

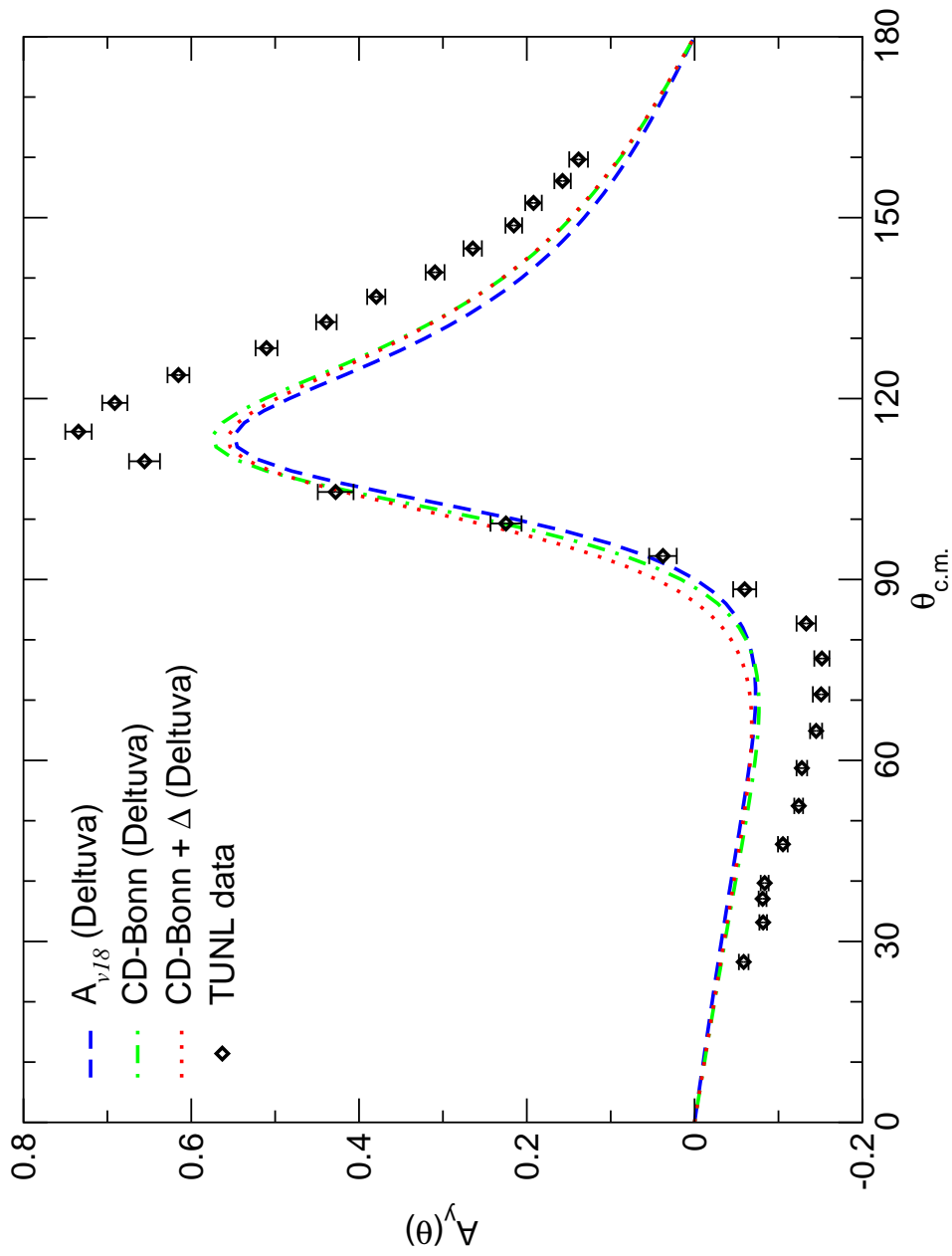


FIGURE 7.5: Measurement and theoretical calculation for the n - ^3He analyzing power at $E_n = 5.54$ MeV as presented in Fig. 7.1.

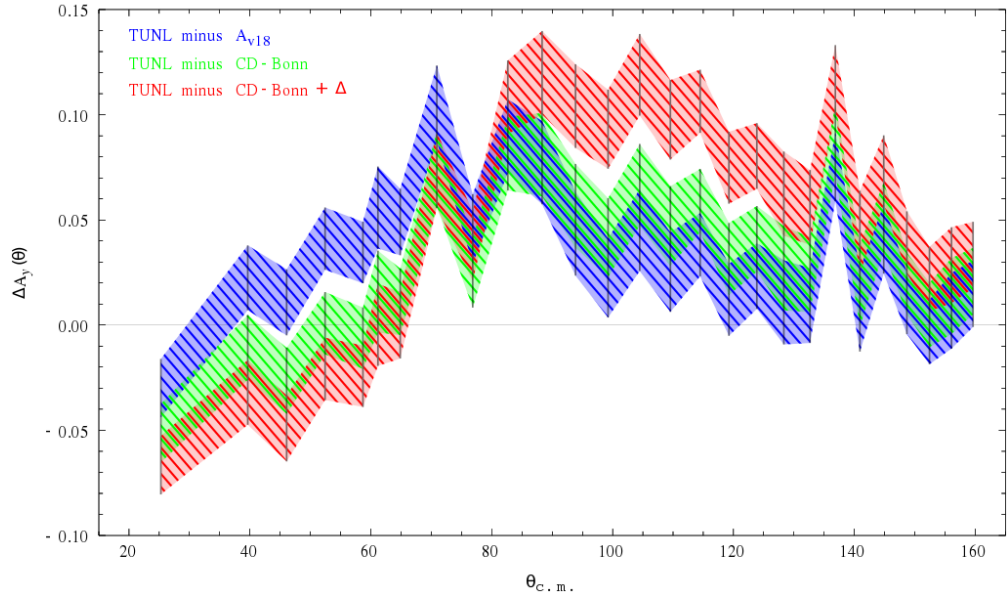


FIGURE 7.6: Differences between experimental and theoretical values of the n - ${}^3\text{He}$ analyzing power at $E_n = 1.60$ MeV (actual values as in Fig. 7.1).

three to two. The closeness of the analyzing powers obtained from the three models at these energies limit the ability to discriminate between them, although this is rendered large irrelevant by the increasing disagreement with measurement.

7.3 Comparison with Previous Measurements

As noted at the outset, previous measurements of the n - ${}^3\text{He}$ analyzing power have been made in the energy range of the present work. A comparison with the results of [Kla85] at $E_n = 3.7$ MeV is shown in Fig. 7.11; a significant difference in the vicinity of the peak is observed between the two measurements, although the lack of prior data at the analyzing power maximum limits the strength of the comparison. It is noted that the liquid ${}^3\text{He}$ target used by [Kla85] required an extensive apparatus, scattering from which (in addition to the much more significant multiple scattering within the liquid helium itself) potentially could have contributed to an artificial lessening of the observed analyzing power that was not compensated by background and Monte Carlo considerations in that work.

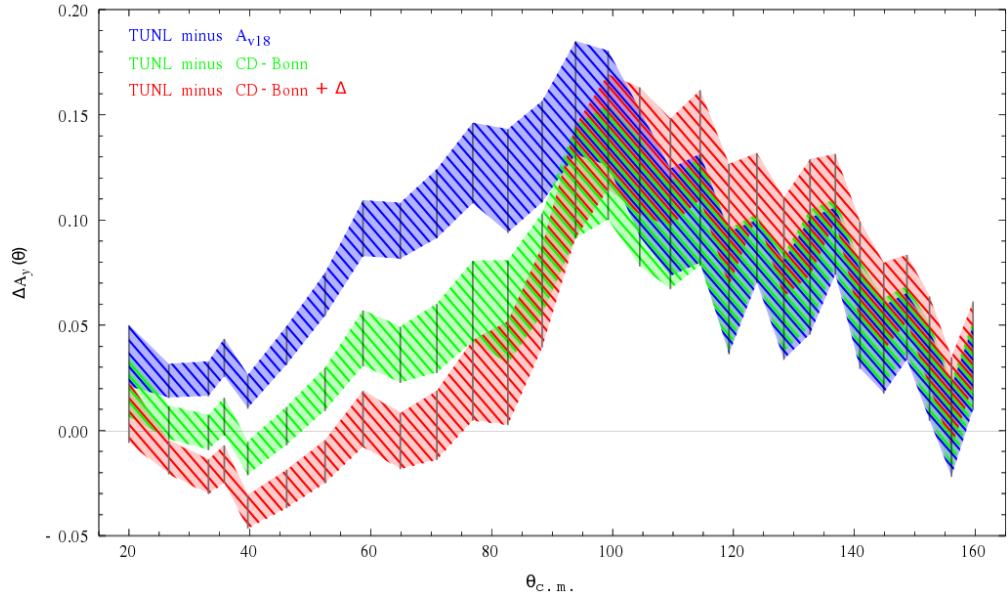


FIGURE 7.7: Differences between experimental and theoretical values of the n - ${}^3\text{He}$ analyzing power at $E_n = 2.26$ MeV (actual values as in Fig. 7.2).

7.4 Comparison with Related Systems

As a measure of the discrepancy between measurement and models, the excess of the experimentally determined analyzing power over theoretical calculations as a proportion of the former for the three $4N$ systems for which analyzing power data is available is presented in Fig. 7.12:

The differences involving the present data are noted to occupy with statistical significance a central place in a trichotomy at around two MeV, with p - ${}^3\text{H}$ measurements in better agreement with theory and p - ${}^3\text{He}$ in worse, with the distinction between the three systems lessened at around five MeV. It is notable that the two systems with mixed total isospin $T = \{0, 1\}$ (namely, p - ${}^3\text{H}$ and n - ${}^3\text{He}$) appear to be in closer agreement between theory and experiment than the pure $T = 1$ p - ${}^3\text{He}$ system.

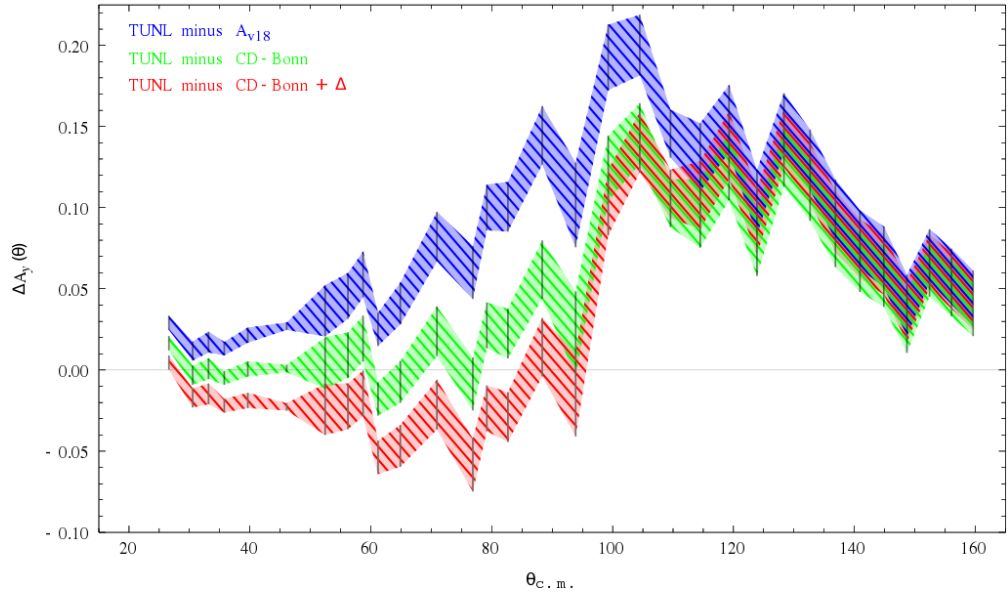


FIGURE 7.8: Differences between experimental and theoretical values of the n - ${}^3\text{He}$ analyzing power at $E_n = 3.14$ MeV (actual values as in Fig. 7.3).

7.5 Summary

A more thorough, and quantitative, comparison between theory and this experiment would be desirable in the form of a phase-shift analysis. Nonetheless, it is firmly established that theoretical calculations have largely failed to accurately predict the present work, the impending publication of which hopefully will contribute to an improvement. An isospin dependence of the differences between theory and experimental data among the four-nucleon systems has been strongly suggested, with the low-energy behaviors in this regard of n - ${}^3\text{He}$ and p - ${}^3\text{He}$ in marked contrast, which in itself may provide insight. Further investigation of this necessitates an inaugural measurement of the n - ${}^3\text{H}$ analyzing power as well as a new experimental determination of the p - ${}^3\text{H}$ analyzing power at low energies. TUNL is currently in the process of securing the tritium required for either of these ventures.

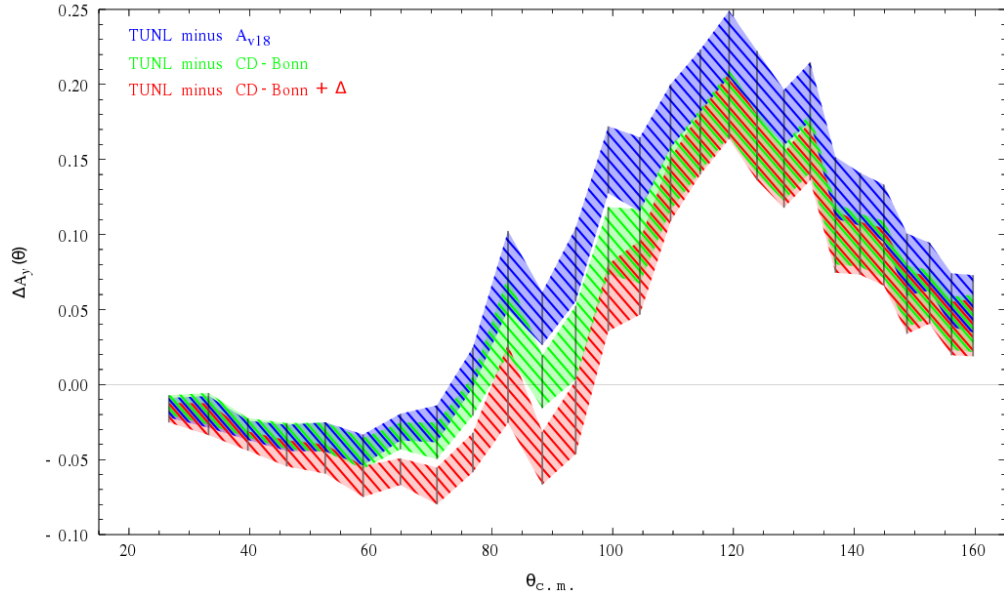


FIGURE 7.9: Differences between experimental and theoretical values of the n - ${}^3\text{He}$ analyzing power at $E_n = 4.05$ MeV (actual values as in Fig. 7.4).

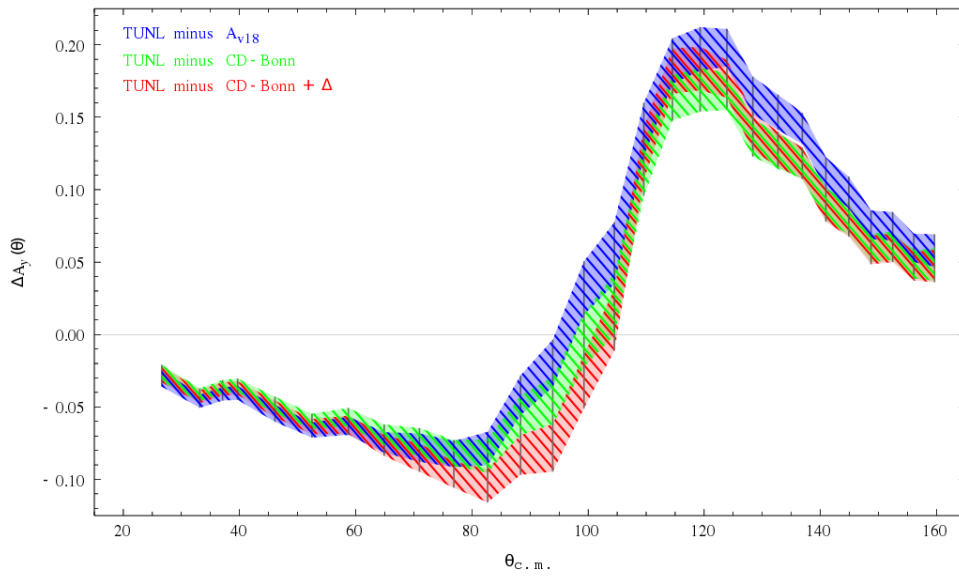


FIGURE 7.10: Differences between experimental and theoretical values of the n - ${}^3\text{He}$ analyzing power at $E_n = 5.54$ MeV (actual values as in Fig. 7.5).

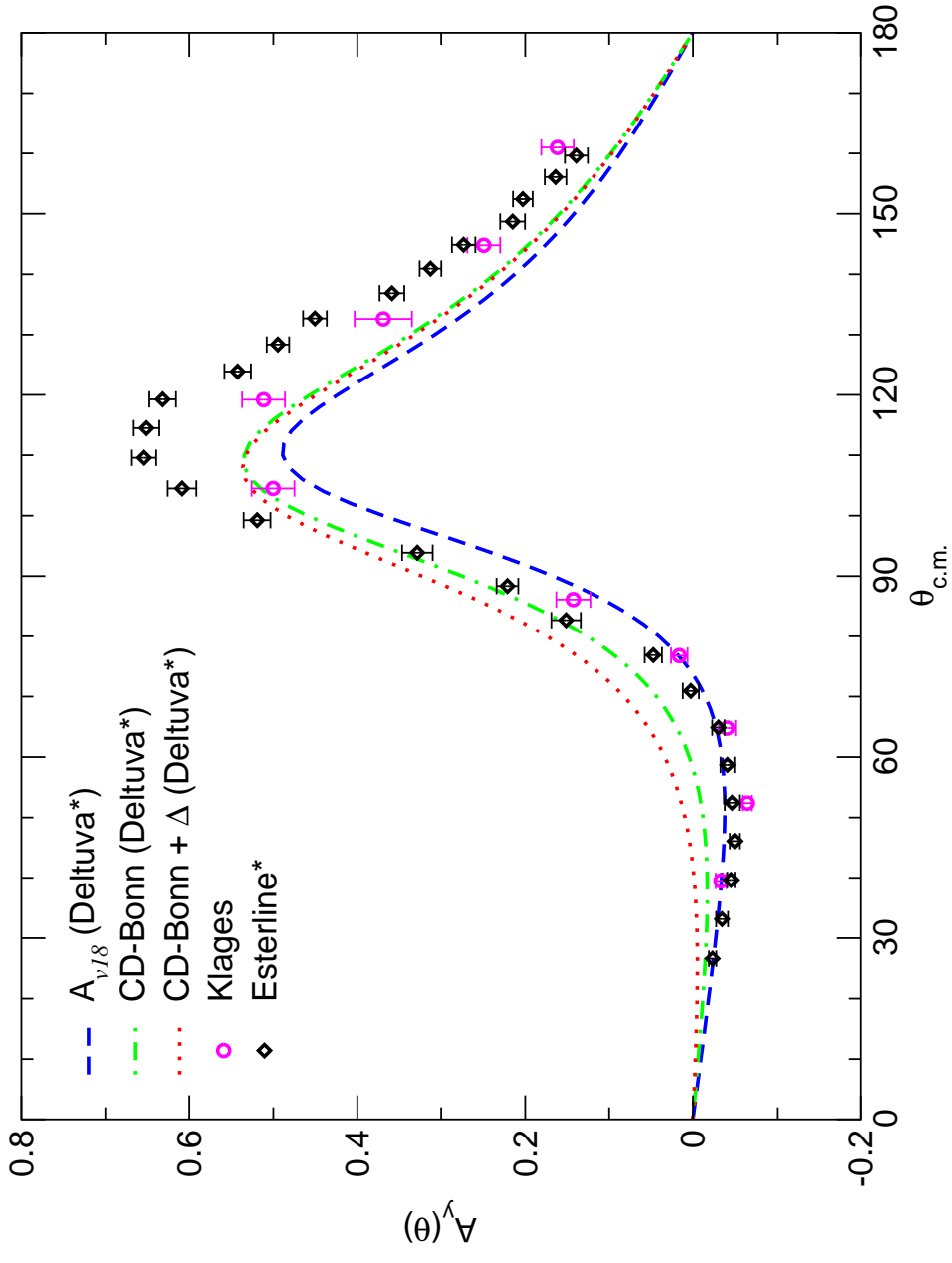


FIGURE 7.11: A linear interpolation between 3.14 and 4.05 MeV data, for angles where data was available at both energies, from the present work (as well as interpolations between corresponding theoretical calculations) and the previous experimental results of [Kla85] at $E_n = 3.7$ MeV.

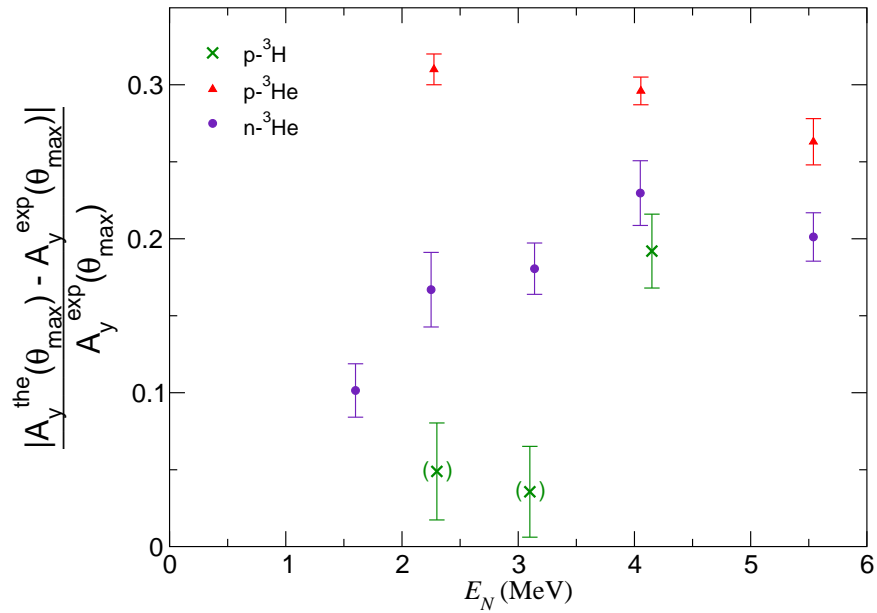


FIGURE 7.12: Differences between experiment and theory in the vicinity of analyzing power maxima as a proportion of the experimental value, obtained by combining the four measurements (and resulting differences with theory) nearest in angle to that corresponding to the analyzing power maximum; E_N is the incident nucleon energy for all three systems: experimental data for $p\text{-}^3\text{He}$ is from [Fis06]; that for $p\text{-}^3\text{H}$ is from [Hal07]; theoretical calculations in all cases are from [Del12]. Parentheses indicate prior unpublished work. Theory underpredicts experiment in all cases.

Bibliography

- [Bra98] R.T. Braun. *The Neutron-Proton Analyzing Power at $E_n = 7.6$ and 12 MeV and the πNN Coupling Constant*. Ph.D. thesis, Duke University, 1998.
- [Del08] A. Deltuva, A.C. Fonseca, and P.U. Sauer. *Four-nucleon system with Δ -isobar excitation*. Physics Letters B, **660**(2008) 471–477.
- [Del12] A. Deltuva, 2012. Private communication.
- [Dri82] L. Drigo, G. Torielli, and G. Zannoni. *Elastic Scattering of Polarized Neutrons by ^3He at Low Energy*. Annalen der Physik, **494**(1982) 408–416.
- [Epe06] E. Epelbaum. *Four-nucleon force in chiral effective field theory*. Physics Letters B, **639**(2006) 456–461.
- [Epe09] E. Epelbaum, H.-W. Hammer, and Ulf-G. Meißner. *Modern theory of nuclear forces*. Reviews of Modern Physics, **81**(2009) 1773–1825.
- [Fis06] B.M. Fischer, C.R. Brune, H.J. Karwowski, D.S. Leonard, E.J. Ludwig, T.C. Black, M. Viviani, A. Kievsky, and S. Rosati. *Proton- ^3He elastic scattering at low energies*. Physical Review C, **74**(2006) 034001.
- [Gra67] P. Grassberger and W. Sandhas. *Systematical Treatment of the Non-Relativistic N -Particle Scattering Problem*. Nuclear Physics B, **2**(1967) 181–206.
- [Hae83] B. Haesner, W. Heeringa, H.O. Klages, H. Dobiach, G. Schmalz, P. Schwarz, J. Wilczynski, B. Zeitnitz, and F. Käppeler. *Measurement of the ^3He and ^4He total neutron cross sections up to 40 MeV*. Physical Review C, **28**(1983) 995–999.
- [Hal07] G. Hale, 2007. Private communication.
- [Hol72] C.E. Hollandsworth, M. Gilpatrick, and W.P. Bucher. *Scattering of Polarized 3 -MeV Neutrons from ^3He* . Physical Review C, **5**(1972) 395–399.

- [Jan88] P. Jany, W. Heeringa, H.O. Klages, B. Zeitnitz, and R. Garrett. *Analyzing Power of n - ^3He Elastic Scattering from 1 to 2 MeV*. Nuclear Physics A, **483**(1988) 269–281.
- [Kie96] A. Kievsky, S. Rosati, W. Tornow, and M. Viviani. *Critical comparison of experimental data and theoretical predictions for N - d scattering below the breakup threshold*. Nuclear Physics A, **607**(1996) 402–424.
- [Kie10] A. Kievsky, M. Viviani, L. Girlanda, and L.E. Marcucci. *Comparative study of three-nucleon force models in $A=3,4$ systems*. Physical Review C, **81**(2010) 044003.
- [Kla85] H.O. Klages, W. Heeringa, H. Dobiasch, R. Fischer, B. Haesner, P. Schwarz, J. Wilczynski, and B. Zeitnitz. *Analyzing Power of the n - ^3He Elastic Scattering from 3.7 to 22.0 MeV*. Nuclear Physics A, **443**(1985) 373–389.
- [Lis76] P.W. Lisowski, T.C. Rhea, R.L. Walter, C.E. Busch, and T.B. Clegg. *Scattering of Polarized Neutrons from ^3He* . Nuclear Physics A, **259**(1976) 61–74.
- [Mar68] J.B. Marion and F.C. Young. *Nuclear Reaction Analysis*. John Wiley and Sons, 1968.
- [Mar02] S. Marrone, D. Cano-Ott, N. Colonna, C. Domingo, F. Gramegna, E.M. Gonzalez, F. Gunsing, M. Heil, F. Käppeler, P.F. Mastinu, P.M. Milazzo, T. Papaevangelou, P. Pavlopoulos, R. Plag, R. Reifarth, G. Tagliente, J.L. Tain, and K. Wisshak. *Pulse shape analysis of liquid scintillators for neutron studies*. Nuclear Instruments and Methods in Physics Research A, **490**(2002) 299–307.
- [Mer98] E. Merzbacher. *Quantum Mechanics*. John Wiley and Sons, third edition, 1998.
- [Nav07] P. Navrátil. *Local three-nucleon interaction from chiral effective field theory*. Few-Body Systems, **41**(2007) 117–140.
- [Rop10] C.D. Roper, T.B. Clegg, J.D. Dunham, A.J. Mendez, W. Tornow, and R.L. Walter. *Improved Results for the $^2\text{H}(d, n)^3\text{He}$ Transverse Vector Polarization-Transfer Coefficient $K_y^y(0^\circ)$ at Low Energies*. Few-Body Systems, **47**(2010) 177–184.
- [Sea60] J.D. Seagrave, L. Cranberg, and J.E. Simmons. *Elastic Scattering of Fast Neutrons by Tritium and He^3* . Physical Review, **119**(1960) 1981–1991.

- [Shi95] S. Shimizu, K. Sagara, H. Nakamura, K. Maeda, T. Miwa, N. Nishimori, S. Ueno, T. Nakashima, and S. Morinobu. *Analyzing powers of $p + d$ scattering below the deuteron breakup threshold*. Physical Review C, **52**(1995) 1193–1202.
- [Tor75] W. Tornow, H. Spiegelhauer, and G. Mack. *Simulation of a Double-Scattering Polarization Experiment with Fast Neutrons by Means of Monte Carlo Calculations*. Nuclear Instruments and Methods, **125**(1975) 373–389.
- [Tor11] W. Tornow, J.H. Esterline, C.A. Leckey, and G.J. Weisel. *High-pressure $^3\text{He-Xe}$ gas scintillators for simultaneous detection of neutrons and gamma rays over a large energy range*. Nuclear Instruments and Methods in Physics Research A, **647**(2011) 86–93.
- [Tor12] W. Tornow, 2012. Private communication.
- [Viv11] M. Viviani, A. Deltuva, R. Lazauskas, J. Carbonell, A.C. Fonseca, A. Kievsky, L.E. Marcucci, and S. Rosati. *Benchmark calculations of $n-^3\text{H}$ and $p-^3\text{He}$ scattering*. Physical Review C, **84**(2011) 054010.

Biography

James Hamilton Esterline

Personal

- Born November 15, 1985 in Minneapolis, Minnesota, United States of America

Education

- B.S. Physics, Mathematics, and Music, Guilford College, Greensboro, North Carolina, United States of America (2003)
- M.A. Physics, Duke University, Durham, North Carolina, United States of America (2005)